

# Electronic Thermal Conductance of Graphene via Electrical Noise

A DISSERTATION PRESENTED  
BY  
JESSE D. CROSSNO  
TO

THE JOHN A. PAULSON SCHOOL OF ENGINEERING AND APPLIED SCIENCES

IN PARTIAL FULFILLMENT OF THE REQUIREMENTS  
FOR THE DEGREE OF  
DOCTOR OF PHILOSOPHY  
IN THE SUBJECT OF  
APPLIED PHYSICS

HARVARD UNIVERSITY  
CAMBRIDGE, MASSACHUSETTS  
MAY 2017

©2014 – JESSE D. CROSSNO  
ALL RIGHTS RESERVED.

Thesis advisor: Professor Philip Kim

Jesse D. Crossno

## Electronic Thermal Conductance of Graphene via Electrical Noise

### ABSTRACT

abstract goes here

# Contents

o INTRODUCTION	I
1 JOHNSON NOISE THERMOMETRY	2
1.1 Thermal noise in resistors . . . . .	3
1.2 Resistor networks: The Johnson noise temperature . . . . .	5
1.3 Johnson noise in RF circuits . . . . .	7
1.4 An autocorrelation RF noise thermometer . . . . .	9
1.5 Uncertainty in noise measurements . . . . .	14
1.6 Impedance matching . . . . .	16
1.6.1 LC tank circuits . . . . .	16
1.6.2 Multi-stage matching . . . . .	21
1.7 Effective noise temperature . . . . .	26
1.8 Calibration . . . . .	30
1.9 Cross-correlated noise thermometry . . . . .	33
1.9.1 multi-terminal cross-correlation . . . . .	36
2 ELECTRONIC COOLING MECHANISMS IN GRAPHENE	38
2.1 Wiedemann-Franz . . . . .	39
2.1.1 Linearization . . . . .	41
2.1.2 Hot-electron shot noise . . . . .	41
2.2 Electron-Phonon coupling . . . . .	42
2.2.1 Linearization . . . . .	43
2.2.2 Bloch-Grüneisen temperature . . . . .	43
2.2.3 Acoustic phonons . . . . .	44
2.2.4 Optical phonons . . . . .	45
2.3 Photon cooling . . . . .	46
2.4 Thermal Network . . . . .	47
3 THERMAL CONDUCTANCE VIA ELECTRICAL NOISE	49
3.1 rectangular device . . . . .	51
3.1.1 Electronic conduction only . . . . .	52
3.1.2 Phonon cooling only . . . . .	55
3.2 Wedge devices . . . . .	55
3.3 Arbitrary geometries: universality of $\beta$ . . . . .	57

3.4	circuitry . . . . .	61
<b>4</b>	<b>HYDRODYNAMIC FRAMEWORK</b>	<b>62</b>
4.1	Hydrodynamic framework . . . . .	62
4.2	Experimental evidence . . . . .	63
<b>5</b>	<b>RF CRYOSTATS AND CIRCUITRY</b>	<b>64</b>
5.1	Janis . . . . .	65
5.2	Oxford . . . . .	65
5.3	Leiden . . . . .	65
5.4	JNT circuits . . . . .	65
<b>6</b>	<b>CALIBRATION OF GRAPHENE DEVICES</b>	<b>66</b>
<b>7</b>	<b>THERMAL CONDUCTANCE IN HIGH DENSITY GRAPHENE</b>	<b>67</b>
7.1	Device characteristics . . . . .	68
7.2	Circuitry . . . . .	68
7.3	Low temperature Wiedemann-franz . . . . .	68
7.4	High temperature electron-phonon . . . . .	68
<b>8</b>	<b>THE DIRAC FLUID</b>	<b>69</b>
<b>9</b>	<b>MAGNETO-THERMAL TRANSPORT</b>	<b>70</b>
<b>10</b>	<b>CONCLUSIONS AND FUTURE WORK</b>	<b>71</b>
<b>REFERENCES</b>		<b>76</b>

THIS IS THE DEDICATION.

# Acknowledgments

I COULD NOT HAVE DONE IT WITHOUT, the help and support of

# 0

## Introduction

outline the basic idea and strict requirements of measuring temperature in 2D systems. Need something non-invasive, layer distinguishing, and electron/phonon distinguishing. Radiation thermometry meets all these requirements. Johnson noise is analogous to this

*In theory, theory and practice are the same thing, but in  
practice...*

Adam Savage

# 1

## Johnson noise thermometry

GIVEN ANY PROCESS IN WHICH AN APPLIED FORCE GENERATES HEAT, the reverse process must also exist and, as such, thermal fluctuations will be create fluctuations in that force. The idea that the same physics governing the dissipation of a object moving through some environment is responsible for the apparent random motion of that object was originally described by Einstein in the context

of pollen grains [12]. The generalized fluctuation-dissipation theorem [21] quantifies this statement for linear systems\* by relating the power spectral density  $S_P(\omega)$  to the real part of the generalized impedance  $Z(\omega)$  [6].

$$S_P(\omega) \propto k_B T \Re[Z(\omega)] \quad (\text{I.1})$$

Nearly a quarter of a century later, Nyquist [26] related Einsteins description of Brownian motion to the electrical noise measured by Johnson [17, 18]. Although all the key components were in place it would take until 1946 for the first noise thermometer to be built [10]. The general idea is to measure the noise spectrum emitted by a device and thus determine its electronic temperature. Johnson noise thermometry (JNT) is analogous to radiation thermometry where the blackbody spectrum of an object is used to determine its temperature — in fact, both rely upon modified versions of eq I.1

## I.I THERMAL NOISE IN RESISTORS

Johnson noise, often referred to as Johnson-Nyquist noise, was first measured in 1927 [17]. Johnson found the fluctuations in the squared voltage across a resistor was linearly proportional to both the resistance and the temperature and independent of the conductor being measured. The following year, Nyquist derived the form of this noise from thermodynamic arguments; consider two identical resistors in thermal equilibrium at a temperature  $T$  connected such that any noise emitted by one is absorbed by the other, as shown in fig. I.I. As we are in equilibrium we know the power being

---

\*Here a linear system is one where the force acting on a particle is proportional to its velocity  $F/v = constant$

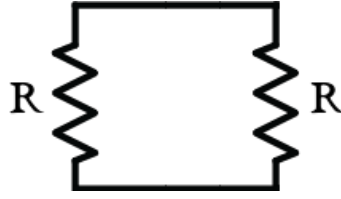


**Figure 1.1:** Schematic of Nyquist's famous thought experiment. Two resistors in thermal equilibrium are connected end to end and allowed to transfer energy between them via thermal current fluctuations.

absorbed per unit frequency must be  $k_B T$ . If we represent the Johnson noise of the first resistor as a series voltage source we know the power dissipated in the second resistor per unit frequency must be  $I^2 R = V_{JN}^2 / 4R$  as the total resistance of the circuit is  $2R$ . Setting this equal to  $k_B T$  leads us to Nyquist's famous result.

$$S_V = 4Rk_B T \quad (1.2)$$

This derivation holds regardless of the conductor, be it an electrolytic solution or a piece of graphene in a quantum Hall state. However, there is a glaring problem with extending this formula to high frequency; similar to the UV-catastrophe in black-body radiation, Nyquist's formula extends to infinite energies as it lacks a high frequency cutoff. This is fixed by quantum mechanics resulting in a cutoff in the noise spectrum centered at  $\hbar\omega = k_B T$ .

$$S_V = 4\hbar\omega \Re(Z) \left[ \frac{1}{2} + \frac{1}{\exp(\hbar\omega/k_B T) - 1} \right] \quad (1.3)$$

This high frequency cutoff was seen experimentally by Schoelkopf, et al. [29] and is only of practical import at high frequencies ( $> 1 \text{ GHz}$ ) and low temperatures ( $< 1 \text{ K}$ ).

## 1.2 RESISTOR NETWORKS: THE JOHNSON NOISE TEMPERATURE

AS NOISE IS A RANDOM PROCESS, adding multiple resistors together into a network is not a simple matter of adding their voltages and/or currents but instead their mean squared voltages  $\langle V^2 \rangle$  and/or mean squared current  $\langle I^2 \rangle$ . This is a property of Gaussian distributed noise: adding together two Gaussian distributions, each with mean 0 and variance  $\sigma$ , with result in another Gaussian distribution with mean 0 and variance  $2\sigma^*$ .

To find the noise emitted by two resistors in series with resistance  $R_1$  and  $R_2$  and temperature  $T_1$  and  $T_2$ , we add their mean squared voltages.

$$\langle V^2 \rangle = 4k_B(R_1 T_1 + R_2 T_2) \Delta f \quad (1.4)$$

While in the case of the same two resistors in parallel we must add their mean squared currents.

$$\langle I^2 \rangle = 4k_B \left( \frac{T_1}{R_1} + \frac{T_2}{R_2} \right) \Delta f \quad (1.5)$$

This process can be extended to any network of discrete, two-terminal resistors.

An effective “Johnson noise temperature” for a given resistor network can be defined as the tem-

---

\*This is why mean squared error is often a useful metric. If errors are unbiased and Gaussian distributed then summing their variance is appropriate

perature,  $T_{JN}$ , such that the total noise emitted between two given terminals of the network is:

$$\langle V^2 \rangle = 4k_B R \Delta f * T_{JN} \quad (1.6)$$

where  $R$  is the two-terminal resistance. For an arbitrary network with many terminals,  $T_{JN}$  will differ depending upon which two-terminals the noise is measured between. For resistors in series we can see from eqn. 1.4

$$\langle V^2 \rangle = 4k_B R \left( \frac{R_1}{R} T_1 + \frac{R_2}{R} T_2 \right) \Delta f \quad (1.7)$$

and thus we can define the Johnson noise temperature for this network as:

$$T_{JN}^{series} = \sum_i \frac{R_i}{R} T_i \quad (1.8)$$

Similarly from eqn.1.5 we see that for resistors in parallel

$$\langle V^2 \rangle = \langle I^2 \rangle \times R^2 = 4k_B R \Delta f \left( \frac{R}{R_1} T_1 + \frac{R}{R_2} * T_2 \right) \quad (1.9)$$

$$T_{JN}^{parallel} = \sum_i \frac{R}{R_i} T_i \quad (1.10)$$

These equations are unified by considering the relationship between the power dissipated in a particular resistor  $\dot{Q}_i$  from a voltage across the two terminals of the network (or equally a current across the network) compared to the total power dissipated over the entire network  $\dot{Q}_0$ . For the

resistors in series  $\dot{Q}_i/\dot{Q}_0 = R_i/R$  and for resistors in parallel  $\dot{Q}_i/\dot{Q}_0 = R/R_i$ . Thus in both cases:

$$T_{JN} = \sum_i \frac{\dot{Q}_i}{\dot{Q}_0} T_i \quad (1.11)$$

In fact this is quite general and holds for any combination of resistors. It stems from the statement: The voltage created on any given two terminals of a resistor network due to the power fluctuations of a given element are exactly given by the power dissipated in that element due to a voltage on those terminals.

In the continuous limit, eqn. 1.11 can be used to find the noise emitted by a device with a spatially non-uniform temperature profile  $T(\vec{r})$  by solving for the spatial power dissipation profile  $\dot{q}(\vec{r})$ .

$$T_{JN} = \frac{\int \dot{q}(\vec{r}) * T(\vec{r}) d\vec{r}}{\int \dot{q}(\vec{r}) d\vec{r}} \quad (1.12)$$

where  $\vec{r}$  is over the spatial dimensions of the device. Eqn. 1.12 is the main result of this section.

### 1.3 JOHNSON NOISE IN RF CIRCUITS

When measuring Johnson noise at high frequency, it can be useful to reformulate the problem into the language of microwave circuits. The Nyquist theorem, eqn. 1.2, can be rewritten to describe the average power,  $\langle P \rangle$ , absorbed by an amplifier coupled to the device with reflection coefficient  $\Gamma^2$ :

$$\langle P \rangle = k_B T \Delta f (1 - \Gamma^2) \quad (1.13)$$

and

$$\Gamma = \frac{Z - Z_0}{Z + Z_0} \quad (1.14)$$

where  $Z$  is the complex impedance of the device and  $Z_0$  is the impedance of the measurement circuit — typically  $50 \Omega$ . In this form it is quite easy to see the thermodynamic origins of the Nyquist equation; A device at temperature  $T$  radiates a power of  $k_B T$  per unit frequency, then some of that power is absorbed by the measurement circuit, and some is reflected back to the sample. All the resistance dependence of the noise power is captured by  $\Gamma^*$ . With this new formulation the importance of minimizing  $\Gamma$  become apparent. For effective high frequency Johnson noise thermometry we must match the impedance of the device to the measurement circuit. For devices with two-terminal resistances far from  $50 \Omega$ , it is beneficial to add impedance matching circuits to transform the device to match  $Z_0$  — in practice resistances less than  $\sim 10 \Omega$  or greater than  $\sim 250 \Omega$  benefit from matching circuits. As can be seen from eqn. 1.13, the larger the measurement bandwidth  $\Delta f$  the larger noise signal. In practice, measurement bandwidths are often limited by either the impedance matching circuitry or the amplifier bandwidth; operating at higher frequencies increases typically increases both these limiting bandwidths.

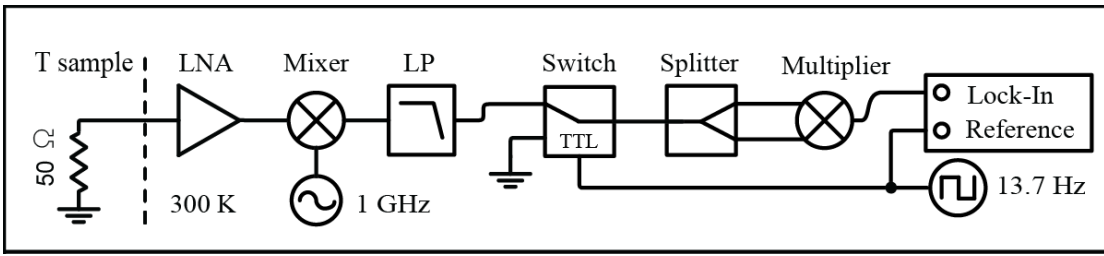


**Figure 1.2:** High level schematic of a typical Johnson noise thermometry measurement circuit. Noise from an impedance matched sample is amplified and a measurement bandwidth is selected using a homodyne mixer and low-pass filter. The noise power is then measured with a power diode or linear multiplier. A microwave switch acts as a chopper and the signal is measured using a lock-in amplifier.

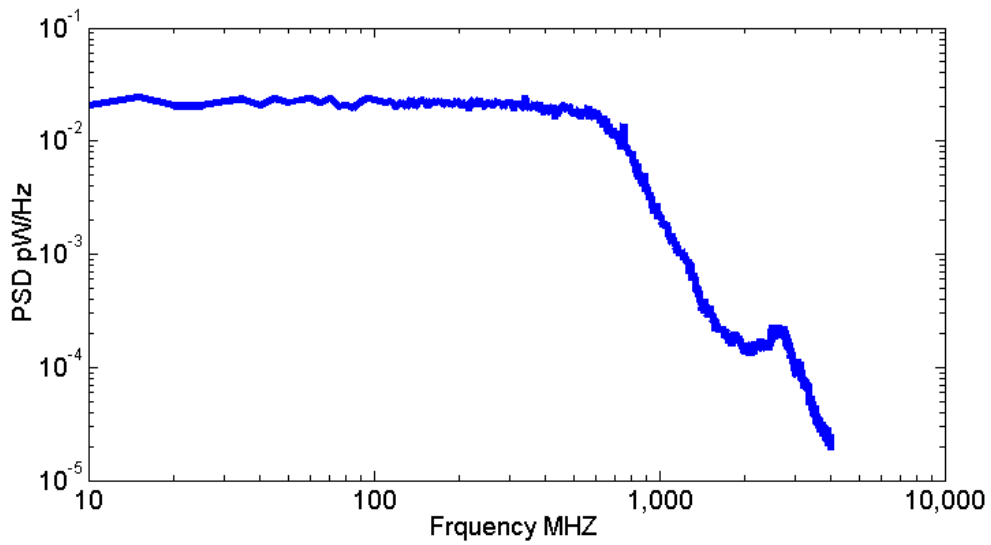
#### I.4 AN AUTOCORRELATION RF NOISE THERMOMETER

Fig. ?? shows an example of a typical, Dicke style, radiometer used to measure the temperature of a  $50\ \Omega$  sample. Radiation from the resistor is coupled into a transmission line terminated in a low noise amplifier (LNA). A typical noise spectrum directly from the output of the LNA is shown in fig. 1.3. The signal-to-noise ratio of a noise measurement is mostly determined the front-end LNA [27] so care should be taken in selecting the right amplifier. The SiGe LNA (Caltech CITLF<sub>3</sub>) used throughout the majority of this thesis has a room temperature noise figure, in the frequency range of 0.01 to 2 GHz, of about 0.64 dB, corresponding to an intrinsic noise temperature of 46 K.

Even though Johnson noise has a flat “white” spectrum, it is important to filter out unwanted  $1/f$  low frequency fluctuations ( $\lesssim 10\ kHz$ ) as well as high frequency noise produced where the amplifier gain begins to roll off. This can be done using high- and low- pass filters (producing a spectrum similar shown in fig. 1.4, or with a homodyne mixer and low-pass filter combo (as shown in fig. ??.

---

\*this is also a nice proof for why  $\Gamma$  in any 2 port device must be symmetric,  $\Gamma_{12} = \Gamma_{21}$ . If this was not true, we could place the device between two resistors in thermal equilibrium and one would heat the other. Two-port devices which report asymmetric coefficients often include internal terminated third ports.



**Figure 1.3:** a typical spectrum directly from the output of a low noise amplifier (Miteq AU-1291  $\sim 65$  dB gain  $\sim 100$  K noise temperature) with the input terminated with a  $50\ \Omega$  resistor. The spectrum is flat until the amplifier gain begins to roll off above 500 MHz. The amplitude of the “white” spectrum is proportional to the resistor temperature added to the amplifier noise temperature.

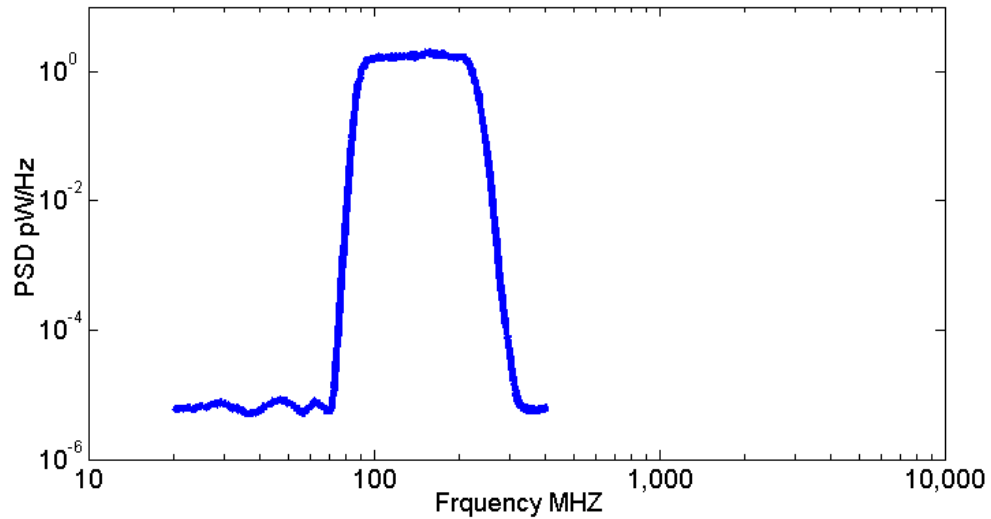


**Figure 1.4:** a typical Johnson noise spectrum after amplification and filtering using SMA high- and low-pass filters (mini-circuits SLP and SHP series). This square band can then integrated to find the total noise power and thus the temperature of the resistor.

Once amplified and cleaned, the total noise power can be measured in a few ways: a spectrum analyzer or digital Fourier transform can read the spectrum directly, a linear multiplier can square the signal and the mean voltage can be measured, or a high frequency power diode and low pass filter combo can convert the power to a DC voltage. Each technique has its own advantages/disadvantages and in a typical experiment multiple techniques are used. When presented with a new device or noise setup a spectrum analyzer is often the first measurement to be done; it provides the most in-depth look into the noise of the system and readily shows problem areas such as narrowband noise, parasitic resonances, and/or amplifier performance. After initial setup, however, spectral detail becomes less important and measurements speeds can be significantly enhanced by moving to an all analog setup.

A linear multiplier (as shown in the schematic fig. 1.2) can be combined with an RF power splitter and a DC voltmeter to directly measure  $\langle V^2 \rangle$ . Operating from DC to 2 GHz, the multiplier, Analog Devices ADL5931, serves as a square law detector with 30 dB dynamic range. A JNT using a multiplier is fast and has the added capability of measuring the autocorrelation function,  $\langle V(t)V(t-\tau) \rangle$ , by simply adding a delay,  $\tau$ , to one arm of the splitter. While more complicated to setup, once operational a multiplier is a good combination of speed and versatility.

The simplest of the three power detectors discussed here is an RF power diode/low-pass filter combo (e.g. Pasternach PE8000-50). These detectors input an RF signal and output a DC voltage as shown in fig. 1.5. The output capacitance of these detectors can be quite large so if a thermal modulation faster than a few 100 Hz is required care must be taken in choosing an appropriate model. Nevertheless, this is the detector used most commonly in the second half of this thesis due to its

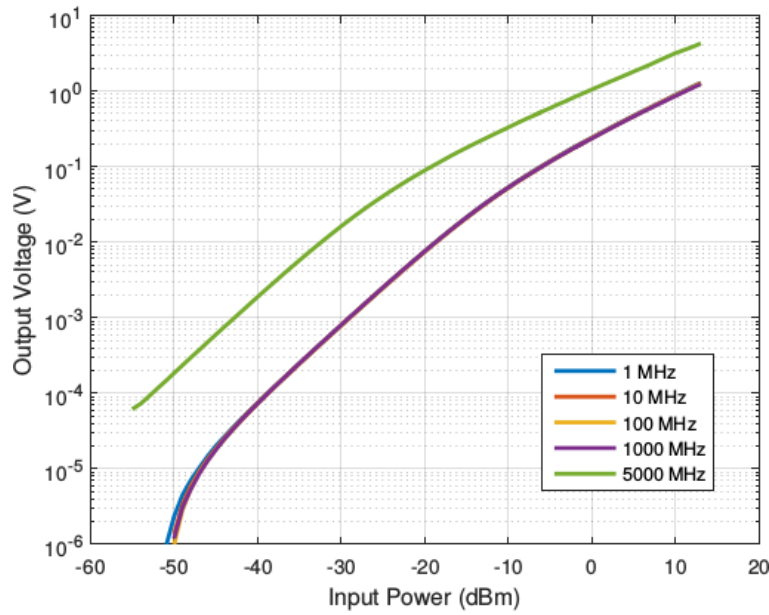


**Figure 1.5:** Calibration curves for the Pasternach PE8000-50 power detector. A monochromatic signal of known power is supplied using a microwave source (Stanford Research Systems) and the output is measured using a Voltmeter (Keithley 2400). The detector has a flat frequency response up to 1 GHz and shows linear behavior from -45 dBm to -25 dBm (30 dB dynamic range)

wide dynamic range (30 dB), small sample package, and ease of use.

Once the noise power is converted to a dc voltage it can be read by a common Voltmeter. To increase the sensitivity it is useful to modulate the noise power. When measuring mesoscopic samples this can be done by modulating the electron temperature via Joule heating. However, in the case of a macroscopic resistor, a microwave switch is placed after amplification and acts as a chopper. The resulting signal can then be measured using a lock-in amplifier.

We can test the noise circuit shown in fig. 1.2 by attaching the sample resistor to a coldfinger and varying the temperature from 3 K to 300 K. The results are shown in fig. 1.26. As the sample temperature is lowered, the noise reduces linearly as expected from eqn. 1.13. However, if we extrapolate the

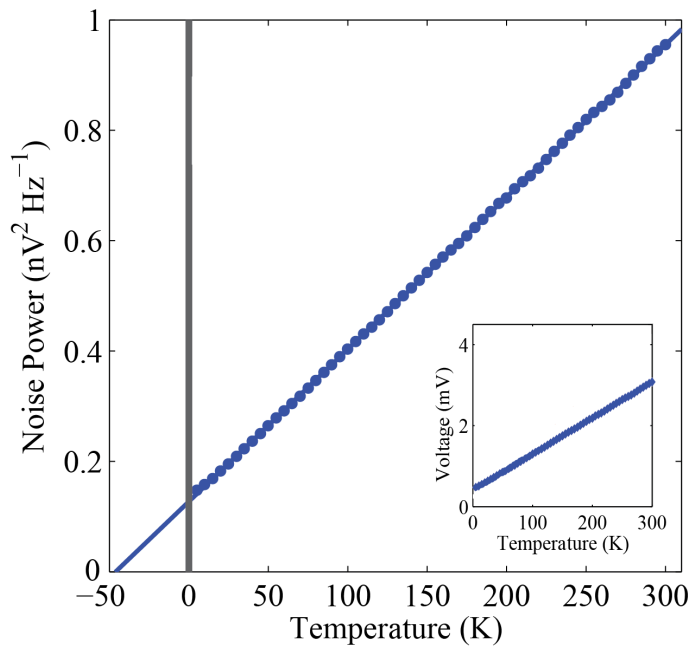


**Figure 1.6:** Johnson noise of a  $50\ \Omega$  resistor measured by the circuit shown in fig. 1.2. Inset show the lock-in amplifier output. The signal is converted to noise power by the Nyquist equation. The solid line is a linear fit with an offset of 68 K due to amplifier noise

data to zero temperature, we see residual noise; this offset is due to all the other (temperature independent) noise sources in the system — primarily the front-end amplifier. It is useful to quantify this offset in units of Kelvin and is called the “effective noise temperature”. Here we find an effective noise temperature of 68 K using a room temperature amplifier. More details on this circuit can be found in ref. [8]

## 1.5 UNCERTAINTY IN NOISE MEASUREMENTS

EVEN NOISE HAS NOISE. There are 2 main areas of uncertainty in a noise measurements: The first comes from the fact that noise is stochastic and deals with how well you know the variance of a Gaussian after measuring some amount of time. If the measurements you take are discrete and uncorrelated then we get the usual  $1/\sqrt{n}$ , but what to do if we are measuring a continuous signal? It turns out this is an old problem which stems back to the 1940 and measurements of noise on telephone lines [? ]. In 1944 Rice showed the effective number of uncorrelated measurements is given by the product of the measurement time  $\tau$  and the effective noise bandwidth\*  $\Delta f$ . This surprising fact that the wider the measurement bandwidth the lower the uncertainty is counter to many experiments where high Q filters are desired to lower the background noise; nevertheless, it can be seen experimentally, as shown in fig. [? ]

The second source of uncertainty comes from external noise sources such as amplifiers and boils down to the question: of the noise you measure, what amount comes from the sample? Quantitatively, this can be thought of as a constant offset to the sample temperature and is called the system noise temperature  $T_n$ <sup>†</sup>. In an autocorrelated noise measurement,  $T_n$  can be estimated as the offset of a linear fit to the noise power vs sample temperature, as shown in fig. 1.26. This offset is primarily

---

\*The effective noise bandwidth is defined as the width of a perfect square band that passes the same noise power as the true filter function.

<sup>†</sup>It should be noted that the system noise temperature can be quite different from an amplifiers intrinsic noise temperature which often assumes a perfectly matched input impedance. See the section “effective noise temperature” for more details

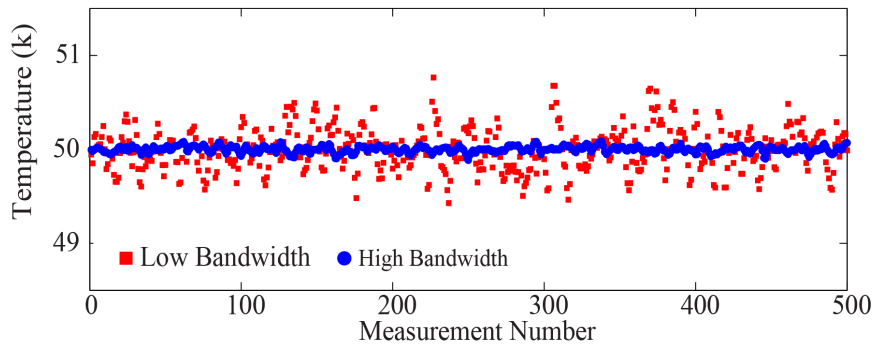


**Figure 1.7:** 500 repeated Johnson noise measurements of a  $50\ \Omega$  resistor at 50 K using two different measurement bandwidths. The high bandwidth data has smaller statistical fluctuations than the low bandwidth data.

due to noise in the front-end amplifier but also depends on the sample impedance matching and the bandwidth being measured.

Combining these two sources of error we arrive at the famous Dicke radiometer formula [10]:

$$\delta T = \frac{T + T_n}{\sqrt{\tau \Delta f}} \quad (1.15)$$

We can directly compare eqn. 1.15 to experiments by repeating a measurement many times and studying how it fluctuates about the mean. Fig. 1.8 compares two histograms, both containing 20,000 autocorrelation measurements at 50 K with 50 ms integration time but using two different bandwidths: 28 and 328 MHz. A sensitivity of 5.5 mK (110 ppm) in 1 second of integration time was achieved using 328 MHz bandwidth on a 50 K signal

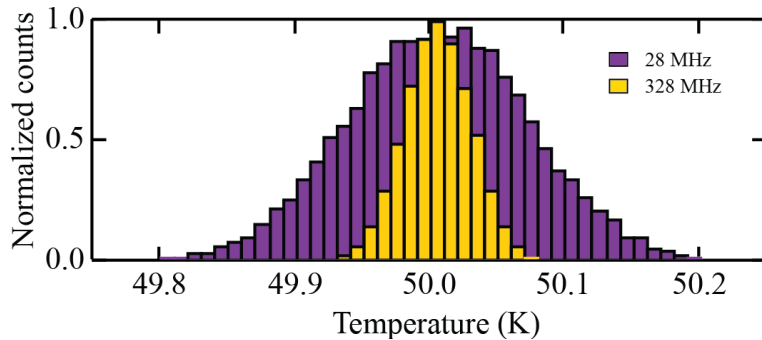


**Figure 1.8:** Histograms of 20,000 auto-correlation temperature measurements for 28 and 328 MHz bandwidth using 50 ms integration time. Histogram peaks are normalized to 1 for clarity. All data is taken on a 50 K resistive load.

## 1.6 IMPEDANCE MATCHING

LIFE DOES NOT ALWAYS GIVE YOU  $50 \Omega$  SAMPLES. Eqn. 1.13 illustrates the importance of minimizing the impedance mismatch between the sample and the measurement circuitry – typically  $50 \Omega$ . The central principle is to use non-dissipative components to transform the total impedance to  $Z(\omega) = 50 + 0i \Omega$  at some frequency  $\omega = 2\pi \times f$ . Impedance matching mesoscopic devices has a unique set of challenges: electrostatic gates and high magnetic fields can cause device impedances to change by multiple orders of magnitude, cryogenic temperatures require the use of only thermally stable components, and large magnetic fields restrict the use of ferrite inductors.

### 1.6.1 LC TANK CIRCUITS

A common way to achieve matching is to use a simple LC circuit. These transformation circuits, known as a tank circuits, can be arranged in several ways but the configuration most useful to these

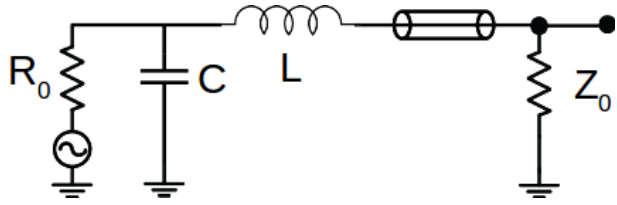


**Figure 1.9:** Schematic of an LC tank circuit setup in a low-pass configuration used to transform a sample resistance  $R_0$  to match the characteristic impedance of a measurement circuit  $Z_0$ .

experiments is that of a low-pass filter — i.e a shunt capacitor followed by a series inductor as shown in fig. [? ]. The impedance of such a circuit is given by:

$$Z(\omega) = (R_0^{-1} + i\omega C)^{-1} + i\omega L \quad (1.16)$$

where  $L$  and  $C$  are the series inductance and shunt capacitance values, respectively. Proper matching requires solving eqn. 1.16 under the condition:

$$Z(\omega_0) = 50 + 0i \Omega \quad (1.17)$$

where  $\omega_0$  is the center of the measurement band. Fig. 1.10 shows a plot of the real and imaginary components of eqn. 1.16 with  $R_0 = 1 k\Omega$ . For the right choice of  $C$  and  $L$ , the imaginary part of the complex impedance crosses 0 when the real part is  $50 \Omega$ . Combining eqn. 1.16 and eqn. 1.17 for a given  $R_0$ ,  $\omega_0$  and  $Z_0$  give us the needed inductance and capacitance values.

$$L = \sqrt{\frac{R_0 Z_0}{\omega_0^2}} \quad C = \frac{1}{\sqrt{R_0 Z_0 \omega_0^2}} \quad (1.18)$$

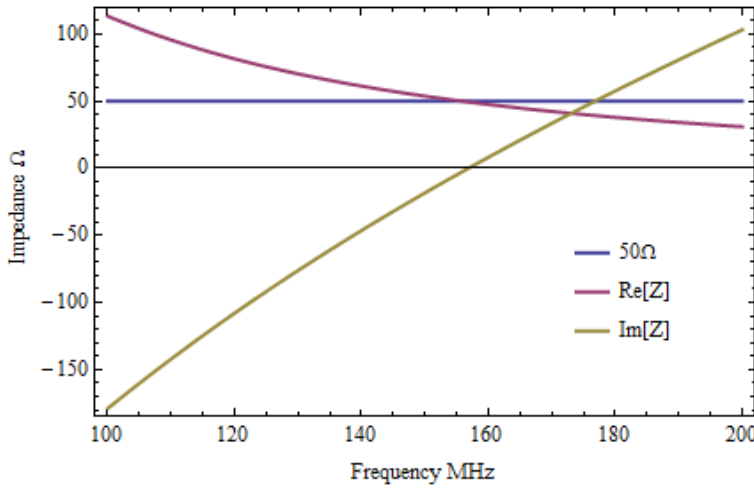


**Figure 1.10:** The real and imaginary impedance of an LC tank circuit (eqn. 1.16) with  $R_0 = 1 \text{ k}\Omega$ ,  $C = 4.5 \text{ pF}$ , and  $L = 220 \text{ nH}$ . The imaginary component cross zero as the real component is  $50 \Omega$ .

While in theory adding a precise induction and capacitance onto a device is straight forward, in practice real devices can have a not insignificant amount of stray capacitance\*. To account for this we can use a variable capacitor and tune the matching circuit to each device. One simple, temperature independent, magnetic field compatible capacitor that can be easily tuned is a set of twisted pair wires. Fig. 1.11 and fig. ?? show an example of a matching circuit using a twisted pair capacitor before and after tuning, respectively.

A vector network analyzer (VNA) is used to measure the sample reflectance  $\Gamma = S_{11}^2$  to ensure the sample is properly matched. Fig. 1.12 shows how the reflectance changes for a  $1 \text{ k}\Omega$  sample impedance and  $220 \text{ nH}$  series inductance as the capacitance is tuned. When properly tuned we measure a large dip in  $S_{11}$  signifying the sample is well coupled to the  $50 \Omega$  VNA.

---

\*stray inductance is also possible (particularly if long wire bonds are necessary) but are usually negligible for the resistance and frequency ranges in this thesis

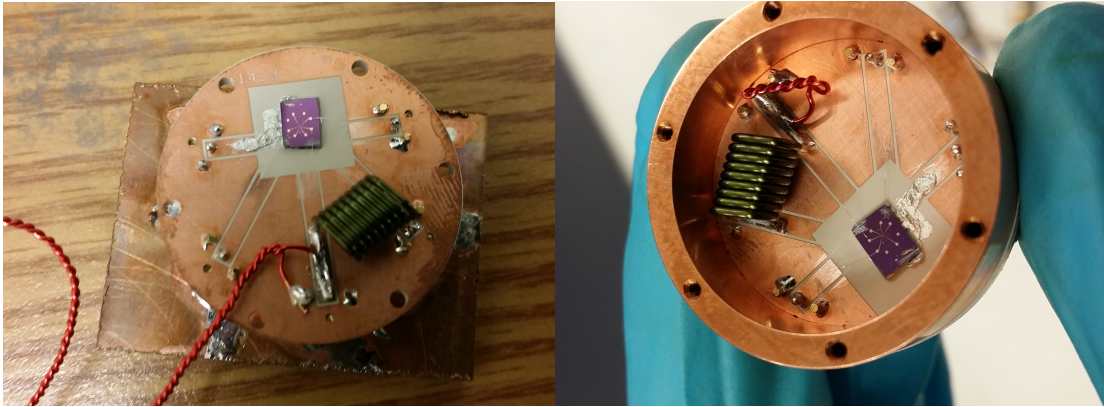


**Figure 1.11:** Images of an impedance matching circuit before (left) and after (right) capacitance tuning. A long piece of twisted pair wire shunts the sample and an inductor (Coilcraft RF Air Core) is placed in series. To tune the capacitance, the twisted pair wire is cut shorter and shorter while the reflectance is monitored.

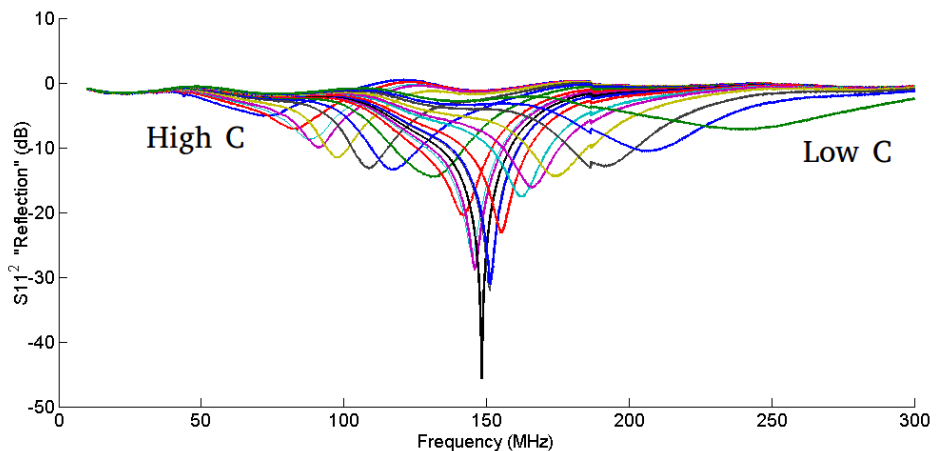


**Figure 1.12:** Reflectance curves while tuning a matching circuit for  $R_0 = 1 \text{ k}\Omega$  and  $L = 200 \text{ nH}$ . The rightmost curve (green) corresponds to the lowest capacitance and the leftmost curve (blue) corresponds to the highest. Each curve is the result of cutting off a section of twisted pair wire.

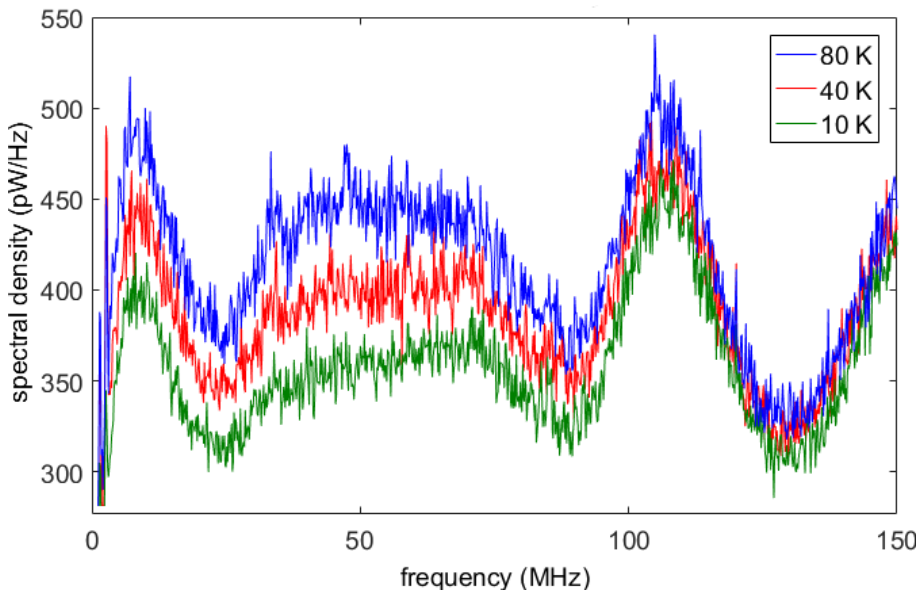


**Figure 1.13:** Amplified noise spectrum from a device, impedance matched using an LC tank circuit, at various temperatures. The background noise is no longer flat as the amplifier is not properly terminated at all frequencies. As the device temperature is raised, the spectral density increases non-uniformly as different frequencies couple differently to the circuitry as determined by eqn. 1.13

After matching, the noise spectral density emitted into the measurement circuitry is no longer flat but instead shaped by  $\Gamma$  in accordance to eqn. 1.13. This point becomes clear when looking at the noise spectra emitted by an impedance matched sample at various temperatures — as shown in Fig. 1.13; two features out prominently: first, the background noise is no longer flat but has structure and, second, the increase in noise as the sample temperature is raised is not the same at all frequencies. The result is that we are no longer free to select just any measurement bandwidth but must carefully choose filters suited to the reflection profile.

In most mesoscopic measurements, the resistance of the device under test varies throughout the experiment; whether electrostatic gates modulate the carrier density, strong magnetic fields drive the system toward quantum hall, or cryogenic temperatures modify the conductivity, matching net-

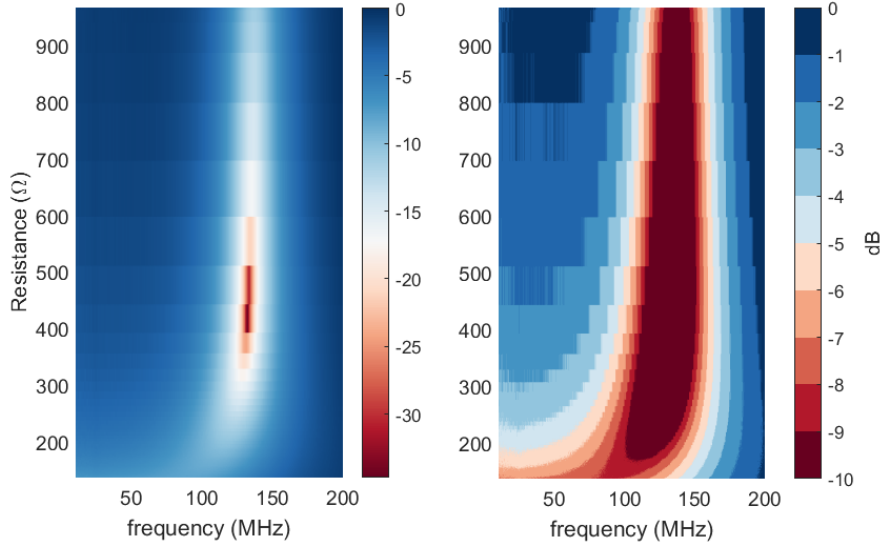


**Figure 1.14:** Reflection coefficient  $|S_{11}|^2$  for a single stage LC matching network as a function of device resistance. The left plot shows the full data set with a maximum coupling efficiency of more than 30 dB. The right plot shows the same data with the color scale adjusted to highlight 1 dB changes up to a maximum of 10 dB (corresponding to 90% coupling efficiency). All data taken from a graphene device at low temperature using an electrostatic gate.

works should operate over a wide dynamic range of input impedances. The response of a single stage LC matching network coupled to a variable resistance device\* is shown in fig. 1.14. The device is optimally matched around  $450 \Omega$  but maintains more than 10 dB coupling between  $200 \Omega$  and  $1 k\Omega$ . As the resistance drops, we see the appearance of the trivial solution to eqn. 1.16 of  $R_0 = 50 \Omega$  and  $\omega = 0$ .

### 1.6.2 MULTI-STAGE MATCHING

Some experiments, such as the magneto-thermal transport studies discussed in chapter 9, require devices to vary in resistance over multiple orders of magnitude. Single stage LC networks are insuf-

---

\*in this case an graphene device with an electrostatic gate

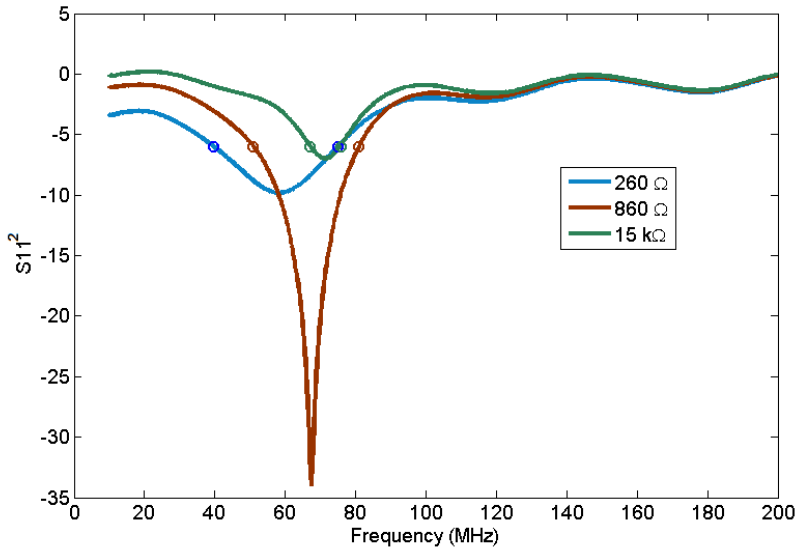


**Figure 1.15:** Reflection measurements of a single stage LC tank circuit coupled to a graphene device at different resistances. At high resistances the coupling drops off and reflection is high.

ficient to cover this wide range. Fig. [?] shows the loss of coupling in a single stage LC tank circuit at high device resistances. In this situation, multiple LC stages can be used to increase the dynamic range.

Multi-stage LC networks allow you to match a wider area of the resistance-frequency space by giving you multiple solutions to the equation  $Z(\omega) = Z_0^*$ . An example schematic of a two-stage LC tank circuit is shown in fig. 1.16. The resulting impedance takes the form:

$$Z(\omega) = \left\{ \left[ (R_0^{-1} + i\omega C_1)^{-1} + i\omega L_1 \right]^{-1} + i\omega C_2 \right\}^{-1} + i\omega L_2 \quad (1.19)$$

---

\*This is a well known solution to a similar problem in audio recording. Multi-stage impedance transforms are used to capture the full audio range [?].

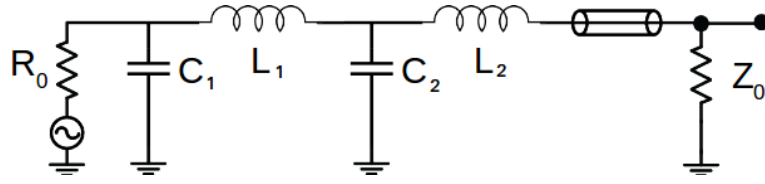


**Figure 1.16:** Schematic of a double-stage LC matching network. The device resistance  $R_0$  is transformed to match the characteristic impedance of the measurement circuit  $Z_0$  using two LC tank circuits. This results in a wider matching bandwidth and/or larger dynamic range depending on the values of the reactive elements.

Eqn. 1.19, under the constraint defined by eqn. 1.17, can have multiple solutions for the same set of inputs. This makes it possible to increase the matching bandwidth for the same dynamic range.

Fig. 1.17 plots the real and imaginary components of eqn. 1.19 for a specific choice of inductances and capacitances designed to cross  $50 + 0i \Omega$  at two nearby frequencies for the same device resistance.

It can be shown for a fixed resistance that the maximum bandwidth occurs when the impedance is dropped by geometric factor [27] — i.e each stage transforms the impedance by the same factor. For an  $N$  stage network of the form shown in fig. 1.16, the  $i$ th inductance and capacitance are given by a generalized form of eqn. 1.18.

$$L_i = \frac{(R_0^{2N-2i+1} Z_0^{2i-1})^{1/2N}}{\omega_0} \quad C_i = \frac{(R_0^{2N-2i+1} Z_0^{2i-1})^{-1/2N}}{\omega_0} \quad (1.20)$$

Applying eqn. 1.20 to a two-stage LC network with a graphene device we can increase the matched bandwidth to  $\sim 150 \text{ MHz}$ , as shown in fig. 1.18.

However, if instead we want to match to larger range of resistances, we can move one of these zeros to a higher resistance. This increases the dynamic range of the matching circuit at the expense of bandwidth. For example, by lowering the first capacitance of the network shown in fig. 1.18, we

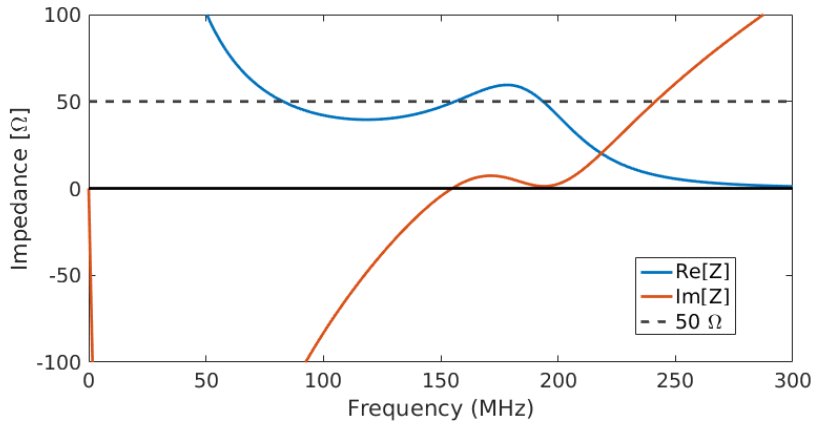


**Figure 1.17:** Real and imaginary components of eqn. 1.19 for  $R = 1000\Omega$ ,  $C_1 = 1.9\text{ pF}$ ,  $L_1 = 430\text{ nH}$ ,  $C_2 = 8.6\text{ pF}$ , and  $L_1 = 96\text{ nH}$ . The impedance goes to  $50 + 0i\Omega$  at two nearby frequencies.

move the high frequency solution from  $\sim 1\text{ k}\Omega$  to  $\sim 4\text{ k}\Omega$ , increasing the dynamic range to include quantum hall resistances, as shown in fig. 1.19.

The more stages added the wider the matched area in resistance-frequency space but also the more sensitive to stray capacitance the circuit becomes. In practice, devices with a  $300\text{ nm SiO}_2$  back-gate dielectric often have  $3 - 6\text{ pF}$  stray capacitance; this can be reduced to less than  $1\text{ pF}$  with the use of insulating substrates and local top-gates, or by increasing the back-gate dielectric to  $1\text{ }\mu\text{m}$ . Reducing the stray reactance also addressed the another challenge that comes with multiple matching stages — it is no longer trivial to tune the circuit using gimmick\*. For these more complicated networks, surface mount ceramic capacitors can be soldered direct to the sample package, as shown in fig. 1.20, and adjustments can be made by careful removal and replacement†

---

\*the twisted pair wire is one form of a gimmick meant to fine tune the circuit capacitance

†making sure not to only the locally to avoid damaging the sample.

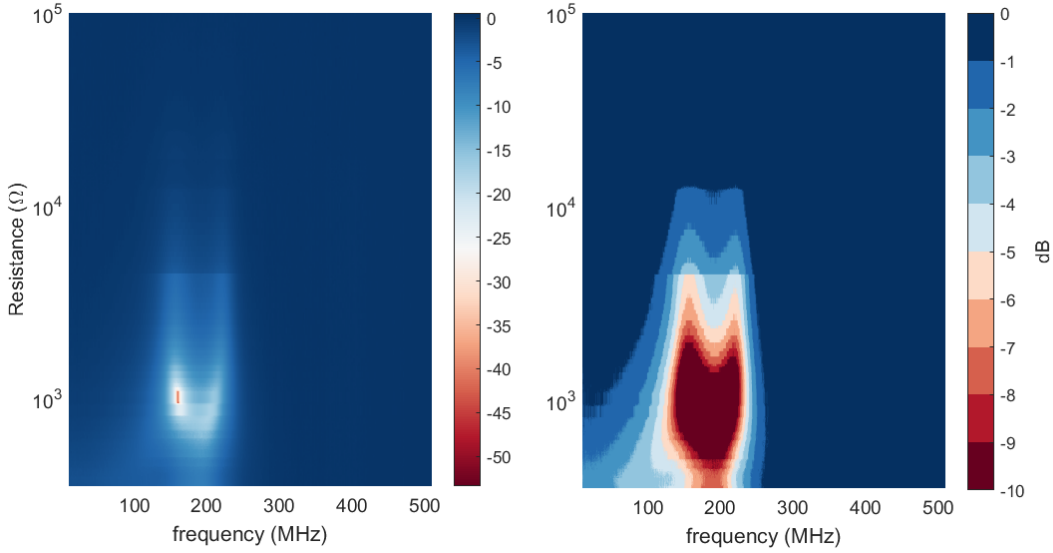


**Figure 1.18:** Reflection coefficient  $|S_{11}|^2$  for a double stage LC matching network as a function of device resistance for reactive components following eqn. 1.20. The left plot shows the full data. The right plot shows the same data with the color scale adjusted to highlight 1 dB changes up to a maximum of 10 dB. The attached graphene device is optimally coupled at  $\sim 1 \text{ k}\Omega$  and has an effective noise bandwidth of  $\sim 150 \text{ MHz}$ .

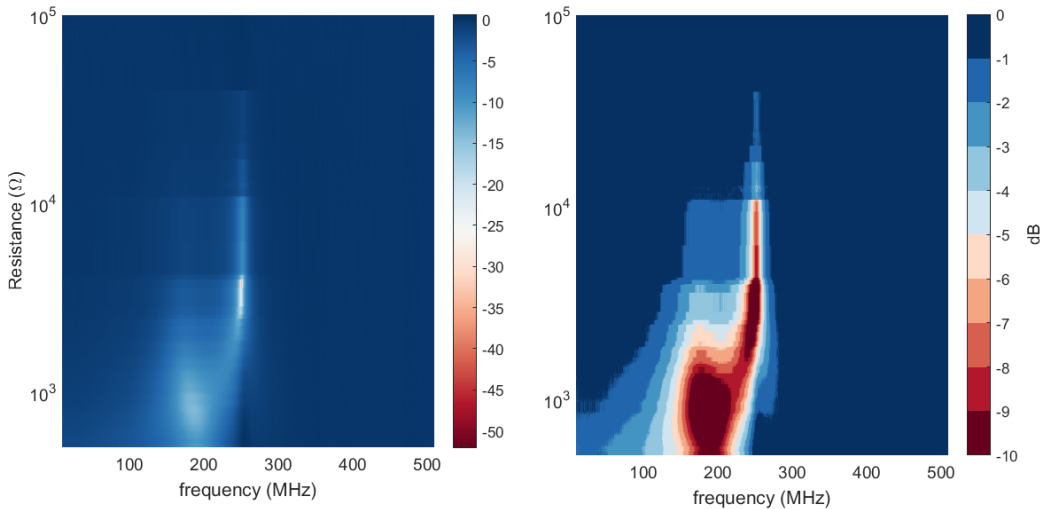


**Figure 1.19:** Reflection coefficient  $|S_{11}|^2$  for the same double stage LC matching network shown in fig. 1.18 as a function of device resistance with the first stage capacitance lowered. This moves the high frequency zero to a higher resistance; effectively increasing the dynamic range at the cost of bandwidth. This technique enables the continuous measurement of graphene devices from zero field into the quantum Hall regime

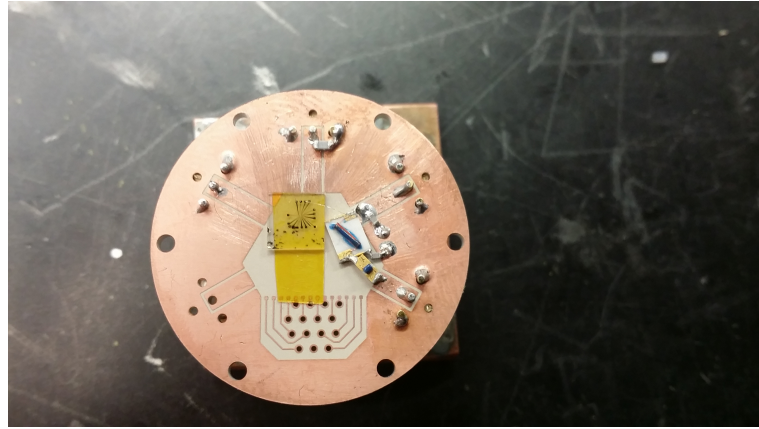


**Figure 1.20:** Image of a two-stage LC matching network soldered directly to a custom cryogenic sample package and wire-bonded to a graphene device. Inductive elements have gold leads allowing direct wire-bonding. The sample is placed on an insulating sapphire substrate with a local top-gate to reduce the stray capacitance.

## 1.7 EFFECTIVE NOISE TEMPERATURE

A FACTOR OF TWO IN SIGNAL TO NOISE CAN BE THE DIFFERENCE BETWEEN GRADUATING IN TWO YEARS OR EIGHT. From the dicke radiometer formula, Eqn. 1.15, the measurement time scales as the effective noise temperature squared. Each component of the measurement circuit should be chosen with this in mind and, as such, its important to understand how each element affects the system as a whole.

The effective noise temperature,  $T_n$ , is the temperature at which your sample emits the same noise power as the sum of all the “unwanted” noise in your system — i.e. your signal to noise ratio is given by  $T/T_n$ , where  $T$  is the sample temperature. Quantifying noise in this way lets us write the

output voltage of our circuit,  $V_{out}$ , (which is proportional to the integrated noise power) as:

$$V_{out} = \mathcal{G}(\Gamma)(T + T_n(\Gamma)) \quad (1.21)$$

where  $\Gamma$  is reflection coefficient between the sample and the amplifier and  $\mathcal{G}$  is the generalized gain factor set by the LNA amplification together with the insertion loss of the microwave components integrated over the bandwidth defined by the external filters. In general, both  $\mathcal{G}$  and  $T_n$  are functions of  $\Gamma$ . All defining characteristics of a given measurement circuit can be swept into  $T_n$  and  $\mathcal{G}$ . In principle these factors must be measured but reasonable estimates can aid in the circuit design.

It is useful to distinguish the difference between the system's intrinsic noise temperature  $T_n^0$  and the system's effective noise temperature  $T_n$ .  $T_n^0$  corresponds to the noise emitted by the circuit relative to the Johnson noise of a perfectly matched resistor, while  $T_n$  is relative to the sample being measured — i.e.  $T_n^0$  can be reported on a device's specification sheet while  $T_n$  is a function of the sample under test and can therefore change with experimental parameters such as electrostatic gate voltage and external field. In general  $T_n$  is always equal to or higher than  $T_n^0$ .

While  $T_n^0$  is primarily determined by the front-end amplifier, every component,  $i$ , with a finite intrinsic noise  $T_i^n$  contributes an amount inversely proportional to the gain before that component,  $G_i$ . For example, if a circuit has three amplification stages with gains  $G_1$ ,  $G_2$ , and  $G_3$  and intrinsic noise temperatures  $T_1^n$ ,  $T_2^n$ , and  $T_3^n$ , respectively, the total system intrinsic noise value is given by:

$$T_n^0 = T_1^n + \frac{T_2^n}{G_1} + \frac{T_3^n}{G_1 G_2} \quad (1.22)$$

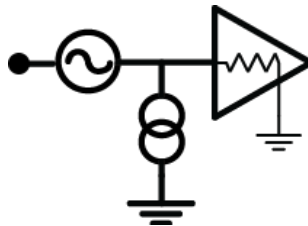


**Figure 1.21:** schematic of a common noise model for active elements. A random voltage source is added in series with the signal and a random current source is added in parallel.

or in general

$$T_n^0 = \sum_i \frac{T_i^n}{\prod_{j < i} G_j} \quad (1.23)$$

hence, if the front-end amplifier has a gain of 30 dB, the noise from second amplifier is effectively reduced by a factor of 1,000.

Estimating  $T_n$  from  $T_n^0$  requires knowing the matching function characterized by  $\Gamma$ . If  $\Gamma$  is frequency independent then  $T_n \approx T_n^0 / (1 - \Gamma)$ . For arbitrary  $\Gamma(\omega)$  you can integrate over the bandwidth defined by external filters  $\Delta f$ \*.

$$T_n \approx \frac{1}{\Delta f} \int_{-\Delta f}^{\Delta f} \frac{T_n^0}{1 - \Gamma(\omega)} d\omega \quad (1.24)$$

The above formulation is approximate as it assumes the system's intrinsic noise can be described entirely by a single parameter  $T_n^0$  — a good assumption if the sample is properly matched. In general, active components require two parameters fully capture the noise behavior. A common tech-

---

\*Eqn. 1.24 approximates the external filter function as a perfect square filter of bandwidth  $\Delta f$ . For the full calculation you must include the full filter function.

nique is to model the circuit with an effective series voltage noise and parallel current noise, as shown in fig. 1.21. However, an equivalent description, which is often more useful in microwave experiments, is that of a forward traveling noise power,  $T_{n,for}^0$ , a reverse traveling noise power  $T_{n,rev}^0$ , and some correlation between them [? ]. In the case of perfect matching,  $\Gamma \rightarrow 0$ ,  $T_{n,rev}^0$  is completely absorbed. However for finite  $\Gamma$  we can write the amplified noise as:

$$\langle P \rangle = G \left( T(1 - \Gamma) + T_{n,rev}^0 \Gamma + T_{n,for}^0 \right) \quad (1.25)$$

Rewriting this in the form of eqn. 1.21 and solving for  $T_n$  and  $G$  yields.

$$T_n(\Gamma) = \frac{\Gamma}{1 - \Gamma} T_{n,rev}^0 + \frac{1}{1 - \Gamma} T_{n,for}^0 \quad (1.26)$$

and

$$G(\Gamma) = \frac{G}{1 - \Gamma} \quad (1.27)$$

While eqn. 1.26 is what determines uncertainty, and therefore the speed of the measurement, an interesting side effect of eqn. 1.25 is that when the sample temperature is equal to  $T_{n,rev}^0$ , the total output noise has no dependence on  $\Gamma$ ; no matter what resistance is being measured, the output noise power is the same! Fig. 1.22 show the total noise power, eqn. 1.25, as a function of sample resistance at several temperatures. The sample is optimally matched at  $\sim 10^3 \Omega$ . In accordance with eqn. 1.25, at low sample temperature the noise decreases as  $\Gamma$  decreases while at high temperature the noise increases as the sample approaches optimal matching. The spacing between curves is proportional to

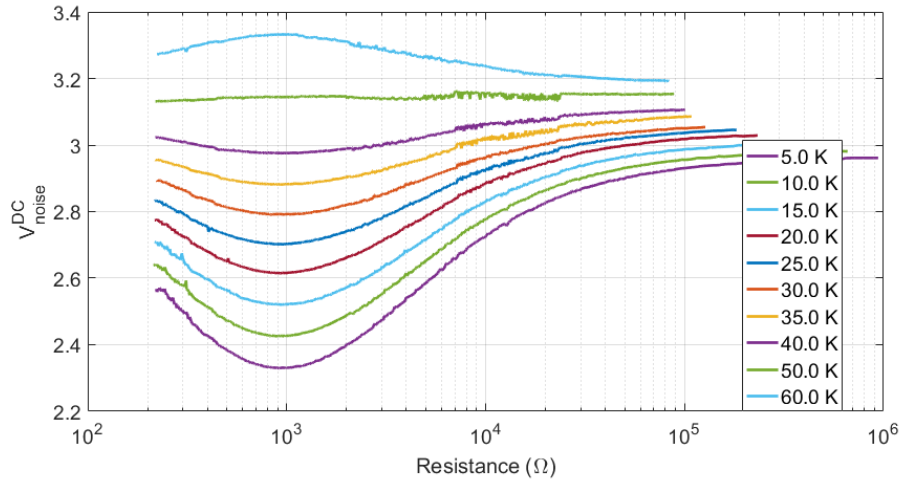


**Figure 1.22:** Voltage proportional to the total integrated noise power as a function of input sample resistance for different sample temperatures. The matching circuit is optimally matched ( $\Gamma$  is minimized) at  $\sim 10^3 \Omega$ . At low temperature, the total noise decreases as  $\Gamma$  decreases, while at high temperature, the opposite is true. At  $T \approx 50 K$  the noise power is constant regardless of the input impedance in accordance with eqn.1.25 and  $T_{n,rev}^0 \approx 50 K$ .

the generalized gain,  $\mathcal{G}(\Gamma)$ , which is maximized when  $\Gamma$  is minimized.

## 1.8 CALIBRATION

CIRCUIT LOSSES AND COUPLINGS ARE DIFFICULT TO CALCULATE A PRIORI, and while  $T_n$  can be modulated away in a differential measurement, the generalize gain  $\mathcal{G}(\Gamma)$  must be calibrated. If the output voltage is written in the form of eqn. 1.21 then  $\mathcal{G}$  is given by:

$$\mathcal{G}(\Gamma) = \left. \frac{dV_{out}}{dT} \right|_{\Gamma} \quad (1.28)$$

The challenge is fixing  $\Gamma$ . If the device under test has a fixed resistance then calibration can be

done by recording  $V_{out}$  for a few select bath temperatures.  $\mathcal{G}$  is then given by the slope of a linear fit to  $V_{out}(T)$ . The inset of fig. 1.26 shows  $V_{out}(T)$  which was used to calibrate  $\mathcal{G}$  yielding the main panel. However, most mesoscopic devices do not have a fixed resistance and thus more care must be taken in calibrating  $\mathcal{G}(\Gamma)$ .

The exact method of calibration will depend on the device characteristics and the size of the parameter space being measured. If impedance of the device is sensitive to external parameters but only has a weak dependence on temperature — i.e.  $|dV_{out}/dT|$  is small and  $V_{out}(T)$  is locally linear on a reasonable experimental scale — then calibration can be done by taking local derivatives of  $V_{out}(T)$  everywhere in the parameter space. While this method is straight forward to implement, it has several glaring drawbacks. Firstly, the time required to find local derivatives for the entire parameter space scales exponentially in the number of parameters. Secondly, it requires knowing the exact parameters that will be measured ahead of time; if during the course of an experiment the parameter space must be expanded or higher resolution is required, calibration must be done again.

A more robust method is to simultaneously measure both  $V_{out}$  and  $\Gamma$  and then numerically solve for  $dV_{out}/dT$  for fixed  $\Gamma$ . Whats more, if the right reactive elements are used for impedance matching,  $\Gamma$  become a function of only the resistance and fixing  $\Gamma$  is equivalent to fixing  $R$ . Fig. 1.22 shows  $V_{out}$  as a function of device resistance for various temperatures. It is important to note that each temperature curve is a collection of many different parameter sweeps that all collapse onto one smooth curve — i.e. it does not matter if the sample is  $13\text{ }k\Omega$  due to electrostatic gating at zero magnetic field, or due to the quantum Hall effect, the emitted noise is the same. If we attempt to fix external parameters and raise the temperature the output voltage nonlinear, but if instead we fix two-

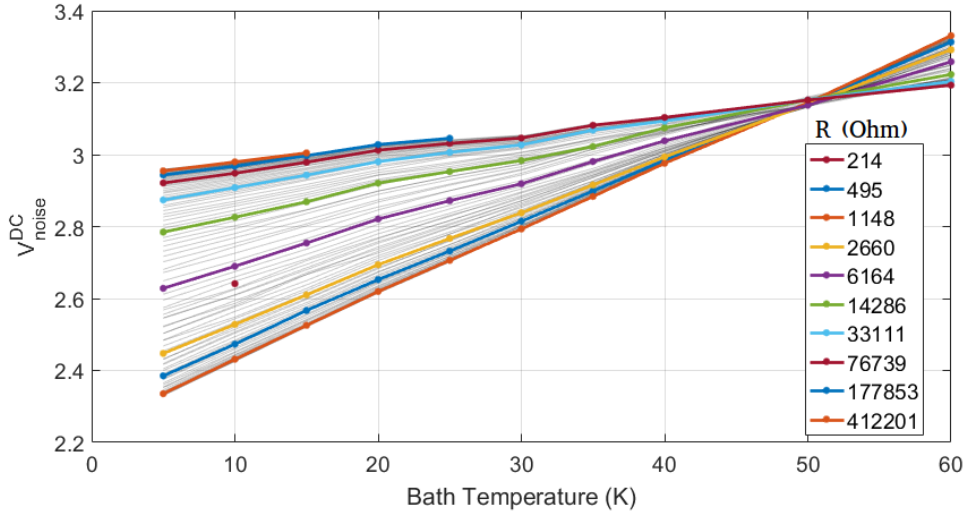


**Figure 1.23:** Output voltage proportional integrated noise given by eqn. 1.21 as a function of device temperature fixing resistance. The slope of each line gives the generalized gain  $\mathcal{G}(R)$  while the extrapolated offset (divided by  $\mathcal{G}$ ) is  $T_n(R)$ . The external parameters that result in a given resistance are generally different for different bath temperatures.

terminal resistance we arrive at fig. 1.23. Linear fits to each line then give  $\mathcal{G}$  as the slope and  $T_n$  as the offset\*. For the data shown in fig. 1.23, the gain and noise temperature is shown in fig. ??; as expected the gain is maximized and the noise temperature is minimized at  $R \sim 1 k\Omega$  where the sample is optimally matched. This particular data was taken from a two-stage matching network coupled to a graphene device and shows a dynamic range of  $\sim 3$  orders of magnitude in device resistance.

---

\*negative  $T_n$  is where the linear fit intercepts the horizontal axis; also given by the offset divided by the slope

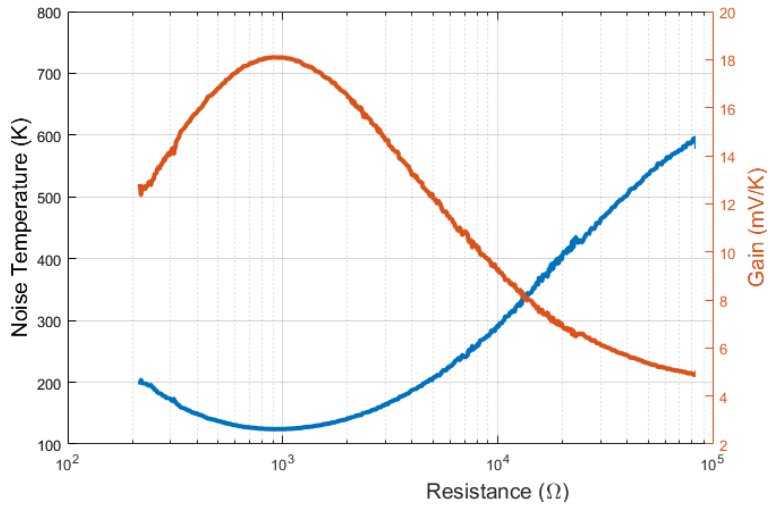


**Figure 1.24:** Generalize gain and effective noise temperature extracted from data shown in fig. 1.23. The circuit is designed to optimally match an input resistance of  $\sim 1k\Omega$ . As expected from eqn. 1.26 and 1.27, the gain is maximized and the noise temperature is minimized when the device is effectively coupled – i.e.  $\Gamma$  is minimized. This two-stage LC tank circuit shows effective coupling over 3 orders of magnitude of input resistance.

## 1.9 CROSS-CORRELATED NOISE THERMOMETRY

A CHALLENGE IN NOISE MEASUREMENTS is isolating the noise you want to measure from the noise you don't. Dissipation between the resistive load and the LNA, such as coaxial attenuation and contact resistance, can contaminate thermal transport measurements [37? ]. Johnson noise from the sample is added to the unwanted Johnson noise from these lossy components. Cross-correlation techniques can mitigate this problem by amplifying the Johnson noise signal of interest independently via two separate measurement lines [? ? ? ? ] and discarding uncorrelated noise between the

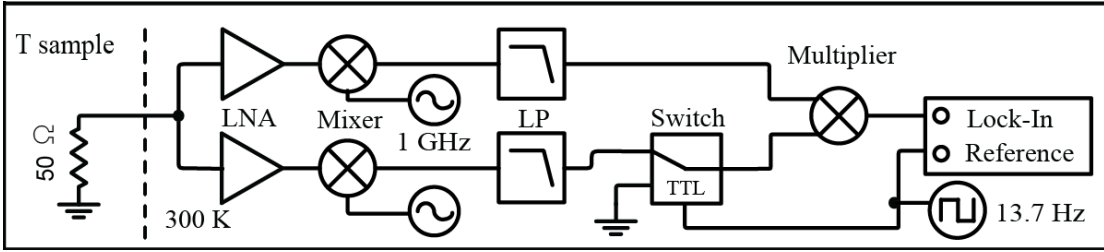


**Figure 1.25:** High level schematic of a typical Johnson noise thermometry cross-correlation measurement circuit. Noise from an impedance matched sample is sent into two independent measurement lines. Each line is then amplified, a measurement bandwidth is selected, and combined using a linear multiplier. A microwave switch acts as a chopper and the signal is integrated using a lock-in amplifier.

two channels. The output voltage of such a scheme can be written as:

$$V_{out} \propto \langle (V_{JN} + V_{n1}) \times (V_{JN} + V_{n2}) \rangle \quad (1.29)$$

$$V_{out} \propto \langle V_{JN}^2 \rangle + \langle V_{JN} V_{n1} \rangle + \langle V_{JN} V_{n2} \rangle + \langle V_{n1} V_{n2} \rangle \quad (1.30)$$

where  $V_{JN}$  is the instantaneous Johnson noise voltage and  $V_{n1}$  and  $V_{n2}$  are the instantaneous voltage noise on the two channels. If all noise sources are uncorrelated then only the first term in eqn. 1.30 is non zero and  $V_{out} \propto \langle V_{JN}^2 \rangle$ . Previously, cross-correlation measurements were limited to frequencies below a few MHz due to the practical implementation of multipliers and digital processing speeds [? ? ? ]. However, the 2 GHz analog multiplier (Analog Devices ADL5931) and LNA, combined with the lock-in amplifier modulation scheme described in fig. 1.25, measure the correlated noise between the two channels, rejecting a large portion of the uncorrelated amplifier noise. The results are shown alongside an autocorrelation measurement (fig. 1.2) for comparison in fig. ??; the offset due to amplifier noise was reduced from 68 K to 2.6 K.

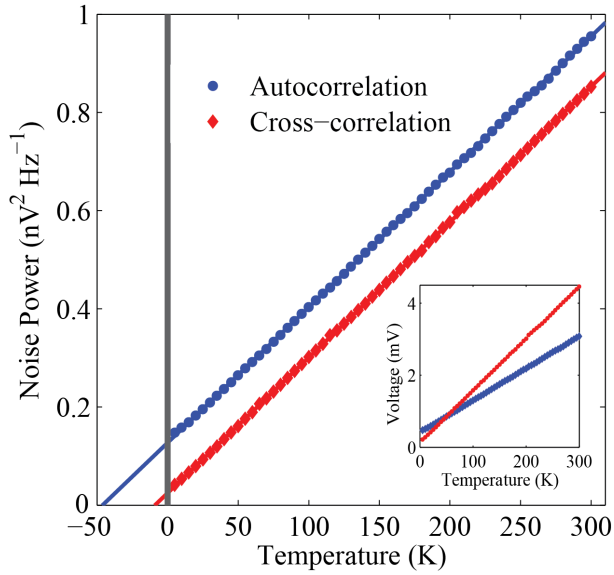


**Figure 1.26:** Auto- and cross-correlation Johnson noise measurements of a  $50\ \Omega$  resistor measured by the circuit shown in fig. 1.2 and 1.25, respectively. Inset shows the raw output voltage. The signal is converted to noise power by the Nyquist equation. The solid lines are linear fits, where the auto- and cross-correlation data exhibit an offset of  $68\ K$  and  $2.6\ K$ , respectively, due to amplifier noise

Although the offset in the data is reduced by cross-correlation, the measurement time required to achieve a given precision is not reduced\*. The time required to effectively average out the uncorrelated noise is still proportional to the amplifiers noise temperature. To be precise,  $T_n$  is given by the geometric mean of individual amplifiers noise temperatures.

$$T_n = \sqrt{T_1^n T_2^n} \quad (1.31)$$

where  $T_i^n$  is the noise temperature of the  $i$ th amplifier. Using two LNAs with similar specifications eqn. 1.31 reduces to the Dicke formula, eqn. 1.15. Fig. 1.27 shows the standard deviation of 1000 tem-

---

\*Cross-correlation can improve the accuracy of an experiment but not the precision

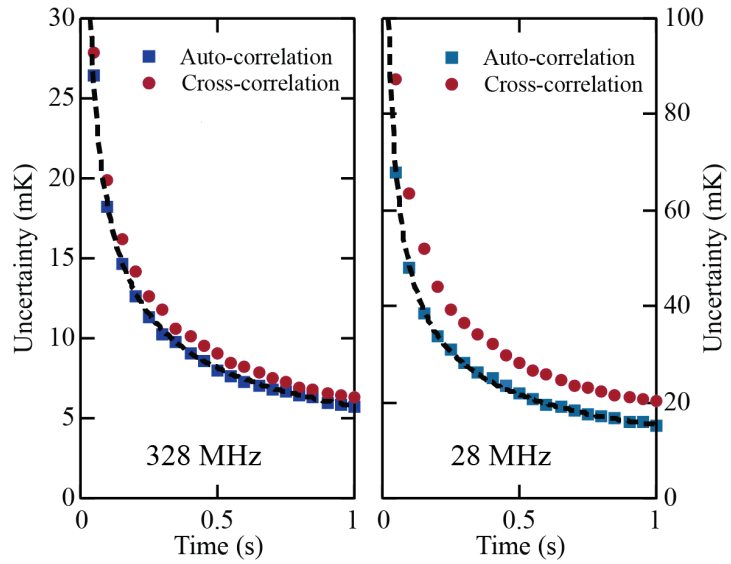


**Figure 1.27:** Standard deviation of 1000 auto- and cross-correlation temperature measurements as a function of integration time for 328 MHz (left) and 28 MHz (right). In all cases, uncertainty follows the Dicke relation, eqn. 1.15, scaling as  $\sqrt{\tau}$  and  $\sqrt{\Delta f}$ . Data is taken from a  $50 \Omega$  resistor

perature measurements as a function of integration time. Both auto- and cross-correlation measurements follow the Dicke formula with similar magnitude and uncertainty scaling as  $\sqrt{\tau}$  and  $\sqrt{\Delta f}$ .

#### 1.9.1 MULTI-TERMINAL CROSS-CORRELATION

Cross-correlation can be used to reduce the effects of contact and lead resistance with the use of multi-terminal devices. However, as discussed in section 1.2, the noise measured on different pairs of terminals sample different areas of the device. For example, the four-terminal device drawn in fig. 1.28 will give very different results depending on which terminal are paired — cross-correlation between  $V_{AD}$  and  $V_{BC}$  will be more sensitive to the device temperature than cross-correlation of



**Figure 1.28:** Cartoon of a four-terminal device. If the voltage between terminals A and D is cross-correlated to the voltage between terminals B and C, the result will be more sensitive to the temperature of the device than pairing A-B and C-D

$V_{AB}$  and  $V_{CD}$ . The exactly amount of overlap between the noise on any pair of terminals

can be found via the method described in section 1.2.

*This is some random quote to start off the chapter.*

Firstname lastname

# 2

## Electronic cooling mechanisms in graphene

CHARGE CARRIERS IN CONDUCTORS exchange energy with the environment in many ways. If an electronic system is directly heated — whether it be by Joule heating, optical pumping, and any other direct energy transfer — the mechanisms with which the system cools can be quite diverse.

In mesoscopic samples there are typically three cooling mechanisms one has to consider. First, if

the material is electrically connected to a thermal bath, such as macroscopic electrodes, then hot electrons can diffuse out and cold electrons can diffuse in; this diffusion is often referred to as Wiedemann-Franz cooling and is the dominate thermal transport mechanism in metals at low temperature [1, 19]. Secondly, hot electrons can transfer energy directly to the lattice by coupling to acoustic and optical phonon modes in the graphene itself or the nearby substrate [? ]. Thirdly, electrons are charged and can therefore radiatively cool; this radiation is often in the form of Johnson noise and, although often negligible even at cryogenic temperature, can be the dominate cooling mechanism in ultra-sensitive bolometers [? ? ].

## 2.1 WIEDEMANN-FRANZ

IF A MATERIAL HOSTS MOBILE CHARGE CARRIERS, at a fixed temperature, each quasiparticle can transport a quantized amount of thermal energy and a quantized charge through the system; it then stands to reason the electronic thermal conductance must be related to the electrical conductivity. First observed at room temperature in 1853 by Wiedemann and Franz [14], the thermal conductivity,  $\kappa$ , of metals is directly proportional to the electrical conductivity,  $\sigma$ , at room temperature. Twenty years later, Lorenz expanded upon the idea and showed the ratio of the thermal conductivity to the product of the electrical conductivity and temperature,  $T$ , was a constant [23],  $\mathcal{L}$ .

$$\frac{\kappa}{\sigma T} = \mathcal{L} \quad (2.1)$$

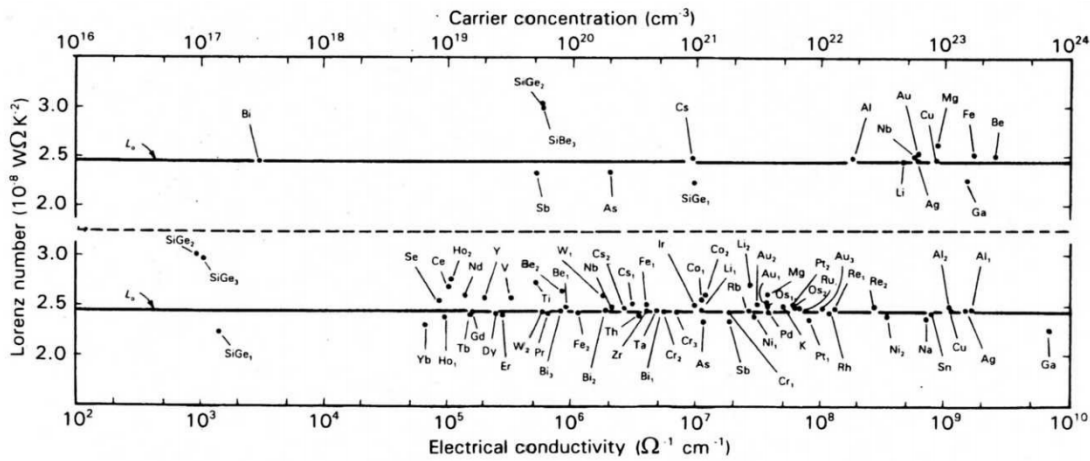


**Figure 2.1:** Experimental Lorentz number of elemental metals and degenerate semiconductors at low temperature. Taken from ref [22]. reprinted with permission, Springer, license number 4067330556225

Eqn. 2.1 is now known as the Wiedemann-Franz law (WFL) where  $\mathcal{L}$  is the Lorenz ratio. Data showing experimentally measured Lorenz numbers for various metals and semi conductors as a function of conductivity and carrier concentration is shown in fig. 2.1. The quantitative value for  $\mathcal{L}$  can be approximated under the Drude model [1] but it was not until Sommerfeld in 1927 that a full derivation using Fermi-Dirac statistics was presented [? ]. Under the assumptions of a degenerate Fermi gas and only elastic collisions, the theoretical value of the Lorenz number was shown to be:

$$\mathcal{L} = \mathcal{L}_0 \equiv \frac{\pi^2}{3} \frac{k_B^2}{e^2} \approx 2.44 \times 10^{-8} \text{ W}\Omega/K^2 \quad (2.2)$$

The requirement that quasiparticles only scatter elastically leads the value of  $\mathcal{L}$  to deviate from  $\mathcal{L}_0$  in the presence of strong electron-electron scattering and inelastic electron-phonon scattering. WF conduction can be suppressed with the use of superconducting leads [25].

### 2.1.1 LINEARIZATION

To understand the behavior of devices under low energy excitations, it is useful to linearize the WFL.

In the linear response regime the temperature variations across a device are small compared to the absolute temperature scale of the problem,  $T_b$ . For a uniform two-dimension device connecting two thermal baths with temperatures  $T_b \pm \Delta T/2$ , the steady state thermal power transported via the WFL is given by:

$$\dot{Q}_{WF} = \left( \frac{W\sigma}{L} \right) \mathcal{L} T_b \Delta T = \frac{\mathcal{L} T_b}{R} \Delta T \quad (2.3)$$

where  $W$  and  $L$  are the sample width and length, respectively, and  $R$  is the two-terminal electrical resistance

### 2.1.2 HOT-ELECTRON SHOT NOISE

A common way to develop a temperature gradient is via Joule heating where the electron temperature is raised with reference to the cold electrodes held at  $T_b$ . In the case of only WF conduction — i.e. no alternative cooling pathways such as phonons — the temperature rise in the high current regime scales linear in the current producing noise very similar to the shot noise seen in vacuum tubes. This well known effect is termed “hot-electron shot noise” [33, 4, 9] and can be seen as the limit of the WFL with  $T_e \gg T_b$ .

$$\dot{Q} \approx \frac{\alpha}{R} T_e^2 \quad (2.4)$$

where  $\alpha$  is a constant related to the temperature profile in the device. If we set the power dissipated to be proportional to the current squared, such that  $\dot{Q} = I^2 R$ , we find:

$$\langle T_e \rangle \approx \frac{R}{\sqrt{\alpha L}} I \quad (2.5)$$

Solving for the temperature profile and the noise produced, eqn. 2.5 reduces to [? ]:

$$S_I = \frac{\sqrt{3}}{4} 2e I \quad (2.6)$$

Eqn.2.6 has the same form as shot noise with Fano factor of  $\sqrt{3}/4$ .

## 2.2 ELECTRON-PHONON COUPLING

At higher temperatures, the cooling of hot electrons is dominated by coupling to acoustic and optical phonons in the hexagonal lattice as well as the nearby substrate [36, 3]. In many experiments involving optical heating or Joule heating, a quasi-equilibrium can be formed where the electron temperature and the lattice temperature can be different. In the particular case of monolayer graphene this is especially true as the high phonon conductivity and relatively weak electron-phonon coupling can result in a lattice temperature that is well sunk to the thermal bath,  $T_b$ , but an elevated electron temperature,  $T_e$ . The interaction between this relativistic fermionic and bosonic system in graphene is quite rich with even the power law for the temperature dependence varying depending on the Fermi level, device disorder, and bias voltage. A general form for the heat transfer between the two

systems can written as:

$$\dot{Q}_{e-ph} = A \Sigma_{e-ph} \left( T_e^\delta - T_b^\delta \right) \quad (2.7)$$

where  $A$  is the area of the device,  $\Sigma_{e-ph}$  is a coupling constant, and  $\delta$  is the power law exponent. Depending on the mechanism  $\delta$  is typically 3 [32, 7] in disordered samples, or 4 – – 5 in clean devices [36, 3]. These relatively high power laws result in phonons dominating at high temperature but becoming negligible when cold.

### 2.2.1 LINEARIZATION

To find the linear response behavior ( $\Delta T \ll T_b$ ) we can Taylor expand to first order for  $T_e \approx T_b$  to find:

$$\dot{Q}_{e-ph} \approx A \delta \Sigma_{e-ph} T_b^{\delta-1} \Delta T \quad (2.8)$$

Eqn. 2.8 can be compared to eqn. 2.3. First we see that while both cooling mechanisms scale as the device width, they have inverse dependences on the device length and as such the bath temperature at which one mechanism will dominate over the other is geometry dependent.

The literature on electron-phonon coupling in graphene is vast [? ? ? 31]. I present here a simplified review of the main mechanisms relevant to the experiments presented here.

### 2.2.2 BLOCH-GRÜNEISEN TEMPERATURE

In most three-dimensional metals, where the Fermi surface is large, the characteristic temperature scale for phonon dynamics is given by the Debye temperature. However, in semiconductors and

semimetals the Fermi surface can be substantially smaller than the Brillouin zone and a second temperature scale governs the scattering of electrons and phonons. The Bloch-Grüneisen temperature,  $T_{BG}$ , is the temperature at which the most energetic phonons have a typical momentum equal to the Fermi momentum [5, 16].

$$T_{BG} = 2\hbar v_s k_F / k_B \quad (2.9)$$

Above this temperature, momentum conservation dictates that only a fraction of the available phonon modes can scatter electrons; the largest momentum change an electron can experience is  $2k_F$  — a complete backscatter — and as such, only phonons with momentum equal to or less than  $2k_F$  can participate in scattering processes. This has been shown in *GaAs* based 2D electron systems [34] and in graphene [11] where  $T_{BG}$  can be controlled by tuning the Fermi level using an electrostatic gate.

### 2.2.3 ACOUSTIC PHONONS

In typical metals at low temperature, the dominate phonon modes in the system are acoustic [1]<sup>\*</sup>. In graphene, however, energy transfer between electrons and these acoustic phonons (AP) is limited by the mismatch between the Fermi velocity,  $v_F$ , and the sound speed in the material,  $v_s$ . Energy and momentum conservation limit the energy each phonon collision can remove from the electronic system resulting a maximal energy transfer of  $2\hbar v_s k_F$ . Nevertheless, experiments have shown that the electronic cooling in many graphene devices at low temperatures can be dominated by AP scatter-

---

<sup>\*</sup>The optical phonon branch has finite energy at  $k = 0$  and thus at low enough temperatures these modes are frozen out

ing [13, 2, 15].

Theoretical predictions for the the power law  $\delta$  and the coupling constant  $\Sigma_{e-ph}$  have been shown to depend upon the device temperature and the amount of disorder. In the dirty limit, the energy and momentum conservation discussed above can be circumvented by disorder-assisted collisions called “supercollisions” resulting in a power law  $\delta = 3$  [32]. In the clean limit at low temperature, Kubakaddi [20] showed  $\delta = 4$  with a coupling constant:

$$\Sigma_{e-ap} = \frac{\pi^2 D^2 |\mu| k_B^4}{15 \rho \hbar^5 v_F^3 v_s^3} \quad (2.10)$$

where  $D$  is the deformation potential,  $\mu$  is the chemical potential, and  $\rho$  is the mass density of the lattice. Eqn. 2.10 was reproduced by Viljas et al. [36] and extended to high temperature where it was found  $\delta$  approaches 5. The transisiton from these two regimes is shown in fig. 2.2.

#### 2.2.4 OPTICAL PHONONS

Although the energies associated with optical phonons in graphene are quite large compared to the thermal energies in typical experiments, each collision can remove a significant amount of energy from the electronic system. Bistritzer et al. [3] showed that at sufficiently high temperatures even the  $\sim 200 \text{ meV}$  intrinsic can dominate electronic cooling in suspended samples. For encapsulated devices, remote phonons in the boron-nitride have been shown to have a surprisingly significant effect both theroretically [36, 3, 24] and experimentally [35]. At higher temperature ( $\gtrsim 270 \text{ K}$ ), Sohier et al. [31] showed that despite the relatively low occupancy, graphene intrinsic optical phonons can

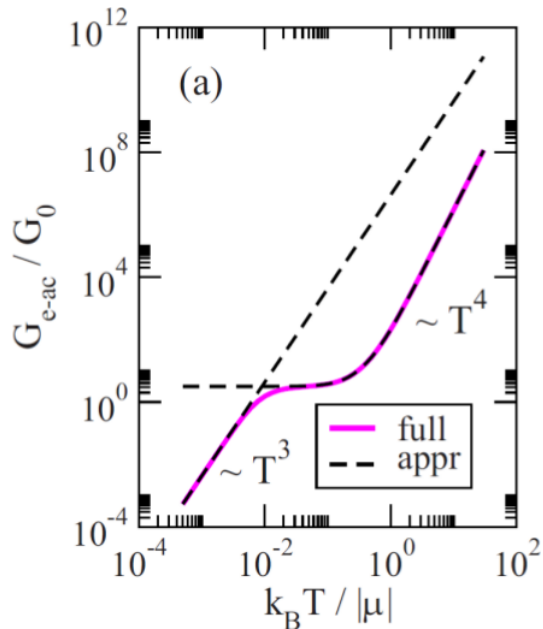


**Figure 2.2:** Reprinted figure with permission from ref. [36] by the American Physical Society license number: 4077361227141.

have a more pronounced effect on the electrical resistance than acoustic phonons.

### 2.3 PHOTON COOLING

For a device coupled to a microwave circuit, energy is radiated via photons over the measurement bandwidth [28, 25]. This is equivalent to 1D blackbody radiation and is the noise which is measured in Johnson noise thermometry. The power transferred is given by eqn. 1.13 which is negligible compared to Wiedemann-Franz and phonon cooling for the temperatures and bandwidths covered in this thesis. However, for devices at low temperature with superconducting leads this can become a significant source of thermalization [25].

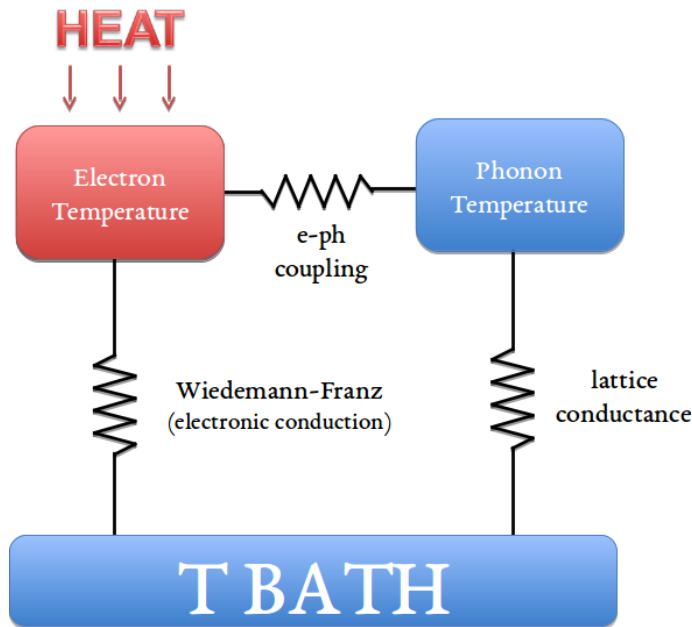


**Figure 2.3:** A thermal model of the electronic cooling pathways in graphene. Heat injected into the electronic system can flow directly to the bath via Wiedemann-Franz conduction, or to the lattice via electron-phonon coupling. The lattice and the bath are connected via the lattice conductivity which is large in graphene.

## 2.4 THERMAL NETWORK

In general, when heat is injected into the electronic system of graphene, each of the mechanisms described above plays a role in thermalizing the system to an external bath. For the devices and experimental parameters used in this thesis, a simplified thermal model can be used, illustrated in fig. 2.3. The electronic system is connected to the bath by two parallel cooling paths: a diffusion channel and a lattice channel. The diffusion channel is governed by the electronic thermal conductivity, while the lattice channel contains both an electron-phonon coupling term and the lattice conductivity of graphene. In practice the lattice conductance is typically many orders of magnitude larger than

the electron-phonon conductance\* resulting in the lattice being well sunk to the bath [8, 13, 30].

The temperature dependence of the two channels follow different power laws resulting in the low temperature behavior being governed by diffusive conduction while cooling at high temperature is dominated by the lattice channel.

---

\*The ratio of the lattice conductance to the electron-phonon conductance is geometry dependent. In long samples the phonon conductance may bottleneck the lattice cooling channel.

# 3

## Thermal conductance via electrical noise

A common technique in studying these cooling pathways is to inject a pulse of energy into the system and monitor the time dependent electron temperature as the system returns to equilibrium.

However, these "pump-probe" experiments suffer from a few difficulties: Firstly, they yield a thermal time constant which is a convolution of the various heat capacities and thermal conductances in the problem. Secondly, the large temperature rise needed to resolve the thermal decay makes it dif-

ficult to study the linear response of low energy excitations. A steady state experiment avoids these difficulties and enables the measurement of thermal conductance in linear response at the expense of time-resolution.

In a steady state thermal experiment, a constant heating power,  $\dot{Q}$ , is injected into the electronic system and the electron temperature rise,  $\Delta T$ , is measured. For the experiments in this thesis, this is accomplished via Joule heating in a two terminal geometry while monitoring the change in Johnson noise temperature,  $T_{JN}$  — as discussed in chapter 1.2. We can define the ratio of the applied power to the rise of Johnson noise temperature as a thermal conductance:

$$G_{\text{th}} = \frac{\dot{Q}}{\Delta T_{JN}} \quad (3.1)$$

It's important to note that  $G_{\text{th}}$  is not the traditional thermal conductance which describes the total heat power flowing through a material in response to a spatial temperature gradient; it is instead a generalized thermal conductance describing the heat power transferred between the electronic system and the bath under Joule heating. To extract meaningful microscopic parameters from  $G_{\text{th}}$  it is necessary model how the heat is entering and leaving the system as a function of these parameters. For the devices and experimental parameters presented here, the simplified thermal model shown in fig. 3.1 can be used to extract information about the electronic thermal conductivity and the electron-phonon coupling.

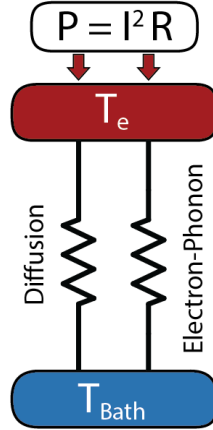


**Figure 3.1:** Simplified thermal diagram of the electronic cooling pathways in graphene relevant for the experimental conditions presented here. A current induces a heating power into the electronic system which conducts to the bath via two parallel pathways: diffusion and coupling to phonons.

### 3.1 RECTANGULAR DEVICE

For a simple two-terminal rectangular device, the temperature measured by Johnson noise — as given by Eqn. 1.12 with spatially uniform  $\dot{q}$  — is simply the spatially averaged temperature. Therefore, the total heat dissipated in linear response is then given by:

$$I^2 R = \dot{Q} = \kappa \left( \frac{W}{L} \right) \beta \Delta T_{\text{JN}} + WL \Sigma_{e-ph} \delta T_b^{\delta-1} \Delta T_{\text{JN}} \quad (3.2)$$

where  $W$  and  $L$  are the sample width and length, respectively,  $T_b$  is the bath temperature,  $\kappa$  is the electronic thermal conductivity,  $\Sigma_{e-ph}$  and  $\delta$  are the electron-phonon parameters described in ch. 2.2, and  $\Delta T_{\text{JN}}$  is the Johnson noise temperature minus the bath temperature. The geometric factor  $\beta$  depends on the shape of the electronic temperature profile which is affected by the relative strength

of the two cooling terms in Eqn. 3.2 and must be calculated.

### 3.1.1 ELECTRONIC CONDUCTION ONLY

In the absence of phonons, the temperature profile, and therefore  $\beta$ , can be solved analytically. For simplicity we assume that the graphene sample is homogeneous, that the approximately uniform electrical current is given by

$$J = -\sigma \frac{dV}{dx} - \alpha \frac{dT}{dx} \quad (3.3)$$

and that the heat current is given by

$$\dot{q} = -\alpha T \frac{dV}{dx} - \bar{\kappa} \frac{dT}{dx} \quad (3.4)$$

where

$$\bar{\kappa} \equiv \kappa + \frac{T\alpha^2}{\sigma} = \kappa(1 + ZT). \quad (3.5)$$

In the latter equation,  $ZT$  is the thermoelectric coefficient of merit. In the limit of negligible thermo electric effects  $\bar{\kappa} \approx \kappa$ .

$dT/dx$  is the temperature gradient in the sample, and  $-dV/dx$  is the electric field in the sample.  $\alpha/\sigma$  is the Seebeck coefficient. If the Joule heating is current biased, the response of graphene is dominated only by the changes in voltage  $V$  and temperature  $T$  to a uniform current density  $J$ , which is applied externally, thus:

$$0 = \frac{dJ}{dx} \quad (3.6)$$

In the linear response regime, the Joule power,  $\mathcal{P}$ , is given by  $\mathbf{J} \times \mathbf{E}$  and thus the continuity equation for the heat current in 1D becomes:

$$\mathcal{P} = \frac{\mathbf{J}^2}{\sigma} = \frac{d\dot{q}}{dx} \quad (3.7)$$

combining the above equations we obtain

$$\mathcal{P} = -\kappa \frac{d^2 T}{dx^2} \quad (3.8)$$

assuming that  $\kappa$  is approximately homogeneous throughout the sample.

The contacts serve as thermal baths and thus are held at the same temperature  $T_b$ . Writing

$$T(x) = T_b + \Delta T(x) \quad (3.9)$$

solving Eqn. 3.1.1 using this form for the solution with the boundary conditions  $\Delta T(0) = \Delta T(L) = 0$  we find a parabolic temperature profile:

$$\Delta T(x) = \frac{\mathcal{P}}{2\kappa} x(L - x) \quad (3.10)$$

The average temperature change in the sample, which is directly measured through Johnson noise thermometry, is

$$\Delta T_{\text{JN}} = \langle \Delta T \rangle = \int_0^L \frac{dx}{L} \Delta T(x) = \frac{\mathcal{P}L^2}{12\kappa} \quad (3.11)$$

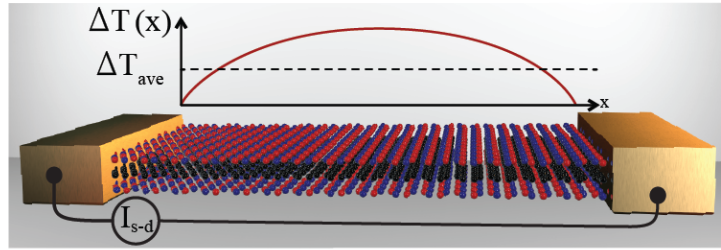


**Figure 3.2:** Cartoon illustrating the non-uniform temperature profile within the graphene-hBN stack during Joule heating in the diffusion-limited regime.

plugging in the power per unit length  $\mathcal{P}$  in terms of  $\sigma$  and the external voltage  $V_0$ ,

$$\Delta T_{\text{JN}} = \frac{V_0^2 \sigma}{12 \kappa} \quad (3.12)$$

This non-uniform temperature profile is illustrated in Fig. 3.2.

Combining eqs. 3.2 and 3.11 in the limit of no electron-phonon coupling we obtain the relation between the experimentally measured  $G_{\text{th}}$  and the microscopic quantity of interest  $\kappa$  as

$$G_{\text{th}} \equiv \frac{\dot{Q}}{\Delta T_{\text{JN}}} = \frac{12W}{L} \kappa \quad (3.13)$$

All the information about the heating profile is contained in the factor of 12. — i.e for a two-terminal rectangular geometry under Joule heating  $\beta = 12$ . If the electronic conductance follows the Wiedemann-Franz law, such that  $\kappa = \mathcal{L}\sigma T$ , then Eqn. 3.13 becomes

$$G_{\text{th}} = \frac{12W\mathcal{L}\sigma T_b}{L} = \frac{12\mathcal{L}T_b}{R} \quad (3.14)$$

where  $R$  is the directly measurable, two-terminal electrical resistance.

### 3.1.2 PHONON COOLING ONLY

The limit of electron-phonon dominated cooling can be modeled by phonons effectively removing an isotropic amount of heat per unit area; the balance between this and Joule heating leads to a uniform temperature profile,

$$\Delta T(x) = T_0 = \Delta T_{\text{JN}} \quad (3.15)$$

The heat balance equation — Eqn. 3.2 with a Joule heating source — then becomes

$$I^2 R = WL \Sigma_{e-ph} \delta T_b^{\delta-1} \Delta T_{\text{JN}} \quad (3.16)$$

and thus the microscopic parameters governing electron-phonon coupling are related to the experimentally measured thermal conductance by

$$G_{\text{th}} = WL \Sigma_{e-ph} \delta T_b^{\delta-1} \quad (3.17)$$

## 3.2 WEDGE DEVICES

Unlike the simple rectangle where the Johnson noise temperature was simply the mean temperature, for more complicated geometries we have to compute what effective temperature we will measure in a noise experiment given the temperature profile. An instructive example of a more complicated

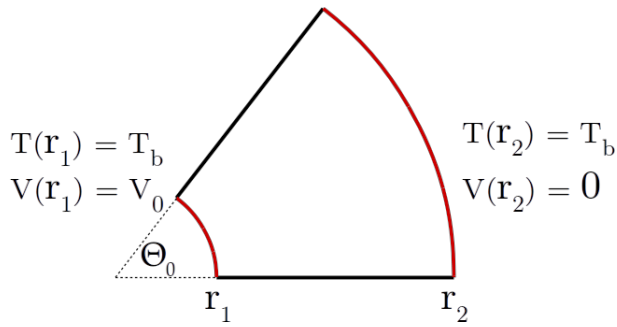


**Figure 3.3:** Sketch of a wedge shaped device and boundary conditions for Joule heating. Red boundaries represent contacts where temperature is fixed at  $T_b$ . A voltage  $V_0$  is placed on the contact at  $r = r_1$  while the second contact at  $r = r_2$  is held at ground. Cylindrical symmetry leaves heat and charge currents independent of angle  $\theta$ .

geometry which can also be solved analytically is a semicircular wedge as shown in fig. 3.3. The continuity equations for heat and charge current in cylindrical coordinates yield

$$J(r) = -\frac{V_0 \sigma}{\ln(r_1/r_2)} \frac{1}{r} \hat{r} \quad (3.18)$$

and

$$\frac{J^2}{\sigma} = \nabla \cdot \dot{q} = \kappa \frac{d^2 T}{dr^2} + \frac{\kappa}{r} \frac{dT}{dr} \quad (3.19)$$

Combining Eqns. 3.18 and 3.19 and solving using the thermal boundary conditions of fixed temperature at the contacts, the temperature profile is given by:

$$\Delta T(r) = \frac{V_0^2 \sigma}{2\kappa \ln(r_1/r_2)^2} \ln\left(\frac{r}{r_1}\right) \ln\left(\frac{r}{r_2}\right) \quad (3.20)$$

The mean temperature and the Johnson noise temperature can be calculated by integrating Eqn. 3.20 yielding,

$$\langle \Delta T \rangle = \int_{r_1}^{r_2} T(r) r dr / \int_{r_1}^{r_2} r dr = \frac{V_0^2 \sigma}{4 \kappa \ln(r_2/r_1)} \left[ \frac{r_1^4 + r_2^4}{r_1^2 + r_2^2} - \ln(r_2/r_1) \right] \quad (3.21)$$

$$\Delta T_{\text{JN}} = \int_{r_1}^{r_2} \dot{q}(r) T(r) r dr / \int_{r_1}^{r_2} \dot{q}(r) r dr = \frac{V_0^2 \sigma}{12 \kappa} \quad (3.22)$$

The difference between the spatially averaged temperature and  $\Delta T_{\text{JN}}$  illustrates the power of combining Joule heating with Johnson noise thermometry — the spatial distribution heat is injected into the system is the same as the spatial weighting function for Johnson noise measurements. Rewriting Eqn. 3.22 in terms of  $G_{\text{th}}$  assuming the Wiedemann-Franz law we arrive at the same form as Eqn. 3.14,

$$G_{\text{th}} = \frac{12 \mathcal{L} T_b}{R} \quad (3.23)$$

All geometric dependence is contained in the experimentally measurable two-terminal resistance  $R$  and we find, similar to the rectangular geometry,  $\beta = 12$ .

### 3.3 ARBITRARY GEOMETRIES: UNIVERSALITY OF $\beta$

Above we have derived two analytic examples where  $\beta$  was shown to 12. In fact, it can be shown that  $\beta = 12$  is universally true in the linear response regime regardless of the geometry of the device or the form of the conductivity tensors,  $\hat{\sigma}$  and  $\hat{\kappa}$ , provided the following conditions are met:

- i. The device has only two electrical terminals which serve as thermal heat sinks

2. Electron cool is provided only by Wiedemann-Franz diffusion
3.  $\hat{\sigma}$  and  $\hat{\kappa}$  are spatially uniform

The following derivation is adapted from a work done by Dr. Brian Skinner, MIT, altered from clarity and brevity:

Without loss of generality, we can imagine a unit voltage applied across an arbitrary two terminal device, so that the electric potential  $\varphi(r)$  has  $\varphi = 1$  at the source electrode and  $\varphi = 0$  at the drain. For a generic conductivity tensor  $\hat{\sigma}$  (which may be affected by magnetic field) the electric current  $\vec{J}(r)$  is

$$\vec{J}(r) = -\hat{\sigma} \vec{\nabla} \varphi. \quad (3.24)$$

Thus, the continuity equation  $\vec{\nabla} \cdot \vec{J} = 0$  becomes

$$\vec{\nabla} \cdot \hat{\sigma} \vec{\nabla} \varphi = 0 \quad (3.25)$$

This equation, together with the boundary conditions, defines the electric potential. The boundaries at non-contact edges are assumed to be reflecting, so that  $(\vec{\nabla} \varphi) \cdot \hat{n} = 0$ , where  $\hat{n}$  is a unit normal vector to the boundary.

The electron temperature  $T(r)$ , defined relative to the base temperature  $T_b$ , obeys the heat diffusion equation

$$\dot{q}(r) = -\vec{\nabla} \cdot (\hat{\kappa} \vec{\nabla} T), \quad (3.26)$$

if there are no extraneous sources of heat dissipation, such as electron-phonon coupling, then the

steady state condition will set  $\dot{q}$  equal to the dissipated Joule heating power per unit area. The Joule power is given by  $\vec{J} \cdot \vec{E}$ , or

$$\dot{q}(r) = (\hat{\sigma} \vec{\nabla} \varphi) \cdot (\vec{\nabla} \varphi) \quad (3.27)$$

If we assume the generalized Wiedemann-Franz relation in the linear response regime,  $\hat{\kappa} = \hat{\sigma} \mathcal{L} T_b$ , we arrive at the following relation governing the temperature:

$$(\hat{\sigma} \vec{\nabla} \varphi) \cdot (\vec{\nabla} \varphi) = -\mathcal{L} T_b \vec{\nabla} \cdot (\hat{\sigma} \vec{\nabla} T). \quad (3.28)$$

Together with the boundary conditions, this equation defines the temperature profile  $T(r)$ . We assume that the contacts are good heat sinks, so that  $T = 0$  at both contacts, and that no heat is lost at the boundary of the sample:  $(\vec{\nabla} T) \cdot \hat{n} = 0$ .

Eqn. 3.28 makes clear that there is a close relation between the temperature profile and the electric potential. It can be shown that Eqn. 3.28 and the boundary conditions are satisfied by the ansatz,

$$T(r) = \frac{1}{2 \mathcal{L} T_b} \varphi(r)(1 - \varphi(r)). \quad (3.29)$$

From Eqn. 3.29 we can calculate the Johnson noise temperature via Eqn. 1.12:

$$\begin{aligned} \Delta T_{\text{JN}} &= \int d^2 r \dot{q}(r) T(r) / \dot{Q} \\ &= \frac{R}{2 \mathcal{L} T_b} \int d^2 r \varphi(r) [1 - \varphi(r)] [\hat{\sigma} \vec{\nabla} \varphi(r)] \cdot [\vec{\nabla} \varphi(r)] \end{aligned} \quad (3.30)$$

Here we have used  $\dot{Q} = V^2/R = 1/R$  (assuming our voltage units). Combining Eqn. 3.29 and 3.30 we can right  $\Delta T_{\text{JN}}$  in terms of only the temperature profile:

$$\begin{aligned} &= \mathcal{L} T_b R \int d^2 r T(r) \vec{\nabla} \cdot (\hat{\sigma} \vec{\nabla} T) \\ &= \mathcal{L} T_b R \int d^2 r (\vec{\nabla} T(r)) \cdot (\hat{\sigma} \vec{\nabla} T(r)). \end{aligned} \quad (3.31)$$

Eqn. 3.31 was found using integration by parts, and noting that either  $T$  or  $\vec{\nabla} T$  vanishes at the boundaries of the sample.

The geometric factor  $\beta$  is defined by

$$\frac{1}{\beta} \equiv \frac{\Delta T_{\text{JN}} \mathcal{L} T_b}{\dot{Q} R}. \quad (3.32)$$

Plugging in Eqn. 3.30

$$\frac{1}{\beta} = \frac{1}{2 \dot{Q}} \int d^2 r \varphi (1 - \varphi) (\hat{\sigma} \vec{\nabla} \varphi) \cdot (\vec{\nabla} \varphi). \quad (3.33)$$

On the other hand, inserting Eqn. 3.29 into eqn. 3.31 and rearranging gives

$$\begin{aligned} \frac{1}{\beta} &= \frac{1}{4 \dot{Q}} \int d^2 r [\vec{\nabla}(\varphi(1 - \varphi))] \cdot [\hat{\sigma} \vec{\nabla}(\varphi(1 - \varphi))] \\ &= \frac{1}{4 \dot{Q}} \int d^2 r (1 - 2\varphi)^2 (\vec{\nabla} \varphi) \cdot (\hat{\sigma} \vec{\nabla} \varphi) \\ &= \frac{1}{4 \dot{Q}} \left[ \int d^2 r (\vec{\nabla} \varphi) \cdot (\hat{\sigma} \vec{\nabla} \varphi) - \int d^2 r 4\varphi(1 - \varphi) (\vec{\nabla} \varphi) \cdot (\hat{\sigma} \vec{\nabla} \varphi) \right]. \end{aligned} \quad (3.34)$$

The second term in Eqn. 3.34 is identical to the right hand side of Eqn. 3.33 multiplied by 2, and it is therefore equal to  $2/\beta$ . Thus:

$$\begin{aligned}
 \frac{1}{\beta} &= \frac{1}{4 \dot{Q}} \int d^2r (\vec{\nabla}\varphi) \cdot (\hat{\sigma} \vec{\nabla}\varphi) \\
 &= \frac{1}{12 \dot{Q}} \int d^2r (\vec{\nabla}\varphi) \cdot (\hat{\sigma} \vec{\nabla}\varphi) \\
 &= \frac{1}{12 \dot{Q}} \int d^2r \dot{q}(r)
 \end{aligned} \tag{3.35}$$

The final step in Eqn. 3.35 comes from realizing the integrand is simply the Joule heating power given in eqn. 3.27, and thus

$$\beta = 12 \tag{3.36}$$

#### 3.4 CIRCUITRY

# 4

## Hydrodynamic framework

explain the problem of transport. Build up historically. Drude. Fermi liquid. Interaction become dominate.

### 4.1 HYDRODYNAMIC FRAMEWORK

inspiration from Subir's old papers and andy's papers

## 4.2 EXPERIMENTAL EVIDENCE

GaAs. Other 2 papers.

# 5

# RF cryostats and circuitry

5.1 JANIS

5.2 OXFORD

5.3 LEIDEN

5.4 JNT CIRCUITS

# 6

## Calibration of graphene devices

# 7

## Thermal conductance in high density graphene

all the data on Aria

7.1 DEVICE CHARACTERISTICS

7.2 CIRCUITRY

7.3 LOW TEMPERATURE WIEDEMANN-FRANZ

7.4 HIGH TEMPERATURE ELECTRON-PHONON

*quote*

Quoteauthor Lastname

# 8

## The Dirac fluid

BLAH BLAH, testing fig. 1.5

*Since the dawn of time, man hath sought to make things  
smaller.*

Eric Bachmann

# 9

## Magneto-thermal transport

THERE'S SOMETHING TO BE SAID for having a good opening line.

# 10

Conclusions and future work

# References

- [1] Ashcroft, N. W. & Mermin, N. D. (1976). *Solid State Physics*. New York: Brooks Cole, 1 edition edition.
- [2] Betz, A. C., Jhang, S. H., Pallecchi, E., Ferreira, R., Fèvre, G., Berroir, J.-M., & Plaçais, B. (2013). Supercollision cooling in undoped graphene. *Nature Physics*, 9(2), 109–112.
- [3] Bistritzer, R. & MacDonald, A. H. (2009). Electronic Cooling in Graphene. *Physical Review Letters*, 102(20), 206410.
- [4] Blanter, Y. M. & Buttiker, M. (2000). Shot Noise in Mesoscopic Conductors. *Physics Reports*, 336(1-2), 1–166. arXiv: cond-mat/9910158.
- [5] Bloch, F. (1930). Zum elektrischen Widerstandsgesetz bei tiefen Temperaturen. *Zeitschrift für Physik*, 59(3-4), 208–214.
- [6] Callen, H. B. & Welton, T. A. (1951). Irreversibility and Generalized Noise. *Physical Review*, 83(1), 34–40.

- [7] Chen, W. & Clerk, A. A. (2012). Electron-phonon mediated heat flow in disordered graphene. *Physical Review B*, 86(12), 125443.
- [8] Crossno, J., Liu, X., Ohki, T. A., Kim, P., & Fong, K. C. (2015). Development of high frequency and wide bandwidth Johnson noise thermometry. *Applied Physics Letters*, 106(2), 023121. arXiv: 1411.4596.
- [9] de Jong, M. J. M. & Beenakker, C. W. J. (1996). Semiclassical theory of shot noise in mesoscopic conductors. *Physica A: Statistical Mechanics and its Applications*, 230(1-2), 219–248. arXiv: cond-mat/9602103.
- [10] Dicke, R. H. (1946). The Measurement of Thermal Radiation at Microwave Frequencies. *Review of Scientific Instruments*, 17(7), 268–275.
- [11] Efetov, D. K. & Kim, P. (2010). Controlling electron-phonon interactions in graphene at ultra high carrier densities. *Physical Review Letters*, 105(25). arXiv: 1009.2988.
- [12] Einstein, A. (2011). *Investigations on the Theory of the Brownian Movement*. Place of publication not identified: BN Publishing.
- [13] Fong, K. C., Wollman, E. E., Ravi, H., Chen, W., Clerk, A. A., Shaw, M. D., Leduc, H. G., & Schwab, K. C. (2013). Measurement of the Electronic Thermal Conductance Channels and Heat Capacity of Graphene at Low Temperature. *Physical Review X*, 3(4), 041008.
- [14] Franz, R. & Wiedemann, G. (1853). Ueber die Wärme-Leitfähigkeit der Metalle. *Annalen der Physik*, 165(8), 497–531.

- [15] Graham, M. W., Shi, S.-F., Ralph, D. C., Park, J., & McEuen, P. L. (2013). Photocurrent measurements of supercollision cooling in graphene. *Nature Physics*, 9(2), 103–108.
- [16] Grüneisen, E. (1933). Die Abhängigkeit des elektrischen Widerstandes reiner Metalle von der Temperatur. *Annalen der Physik*, 408(5), 530–540.
- [17] Johnson, J. B. (1927). Thermal Agitation of Electricity in Conductors : Abstract : Nature. *Nature*, 119(2984), 50–51.
- [18] Johnson, J. B. (1928). Thermal Agitation of Electricity in Conductors. *Physical Review*, 32(1), 97–109.
- [19] Kittel, C. (2004). *Introduction to Solid State Physics*. Hoboken, NJ: Wiley, 8 edition edition.
- [20] Kubakaddi, S. S. (2009). Interaction of massless Dirac electrons with acoustic phonons in graphene at low temperatures. *Physical Review B*, 79(7), 075417.
- [21] Kubo, R. (1966). The fluctuation-dissipation theorem. *Reports on Progress in Physics*, 29(1), 255.
- [22] Kumar, G. S., Prasad, G., & Pohl, R. O. (1993). Experimental determinations of the Lorenz number. *Journal of Materials Science*, 28(16), 4261–4272.
- [23] Lorenz, L. (1872). Bestimmung der Wärmegrade in absolutem Maasse. *Annalen der Physik*, 223(II), 429–452.

- [24] Low, T., Perebeinos, V., Kim, R., Freitag, M., & Avouris, P. (2012). Cooling of photoexcited carriers in graphene by internal and substrate phonons. *Physical Review B*, 86(4), 045413.
- [25] McKitterick, C. (2015). *Prospects for Ultra-sensitive Terahertz Photon Detection with Graphene*. PhD thesis, Yale University.
- [26] Nyquist, H. (1928). Thermal Agitation of Electric Charge in Conductors. *Physical Review*, 32(1), 110–113.
- [27] Pozar, D. M. (2011). *Microwave Engineering*. Hoboken, NJ: Wiley, 4 edition edition.
- [28] Schmidt, D. R., Schoelkopf, R. J., & Cleland, A. N. (2004). Photon-Mediated Thermal Relaxation of Electrons in Nanostructures. *Physical Review Letters*, 93(4), 045901.
- [29] Schoelkopf, R. J., Burke, P. J., Kozhevnikov, A. A., Prober, D. E., & Rooks, M. J. (1997). Frequency Dependence of Shot Noise in a Diffusive Mesoscopic Conductor. *Physical Review Letters*, 78(17), 3370–3373.
- [30] Seol, J. H., Jo, I., Moore, A. L., Lindsay, L., Aitken, Z. H., Pettes, M. T., Li, X., Yao, Z., Huang, R., Broido, D., Mingo, N., Ruoff, R. S., & Shi, L. (2010). Two-Dimensional Phonon Transport in Supported Graphene. *Science*, 328(5975), 213–216.
- [31] Sohier, T., Calandra, M., Park, C.-H., Bonini, N., Marzari, N., & Mauri, F. (2014). Phonon-limited resistivity of graphene by first-principles calculations: Electron-phonon interactions, strain-induced gauge field, and Boltzmann equation. *Physical Review B*, 90(12), 125414.

- [32] Song, J. C. W., Reizer, M. Y., & Levitov, L. S. (2012). Disorder-Assisted Electron-Phonon Scattering and Cooling Pathways in Graphene. *Physical Review Letters*, 109(10), 106602.
- [33] Steinbach, A. H., Martinis, J. M., & Devoret, M. H. (1996). Observation of Hot-Electron Shot Noise in a Metallic Resistor. *Physical Review Letters*, 76(20), 3806–3809.
- [34] Stormer, H. L., Pfeiffer, L. N., Baldwin, K. W., & West, K. W. (1990). Observation of a Bloch-Gr\"uneisen regime in two-dimensional electron transport. *Physical Review B*, 41(2), 1278–1281.
- [35] Tielrooij, K. J., Hesp, N. C. H., Principi, A., Lundeberg, M., Pogna, E. A. A., Banszerus, L., Mics, Z., Massicotte, M., Schmidt, P., Davydovskaya, D., Watanabe, K., Taniguchi, T., Bonn, M., Turchinovich, D., Stampfer, C., Cerullo, G., Polini, M., & Koppens, F. H. L. (2017). Out-of-plane heat transfer in van der Waals stacks: electron-hyperbolic phonon coupling. *arXiv:1702.03766 [cond-mat]*. arXiv: 1702.03766.
- [36] Viljas, J. K. & Heikkil\"a, T. T. (2010). Electron-phonon heat transfer in monolayer and bilayer graphene. *Physical Review B*, 81(24), 245404.
- [37] White, D. R., Galleano, R., Actis, A., Brixy, H., Groot, M. D., Dubbeldam, J., Reesink, A. L., Edler, F., Sakurai, H., Shepard, R. L., & Gallop, J. C. (1996). The status of Johnson noise thermometry. *Metrologia*, 33(4), 325.